

North-South and Vertical Deformation Across the Western Anatolian Extensional Province (Türkiye) from Sentinel-1 InSAR

Manuel Diercks¹, Ekbal Hussain², Zoë K. Mildon¹, Sarah J. Boulton¹, Milan
Lazecký³

¹School of Geography, Earth and Environmental Sciences, University of Plymouth, Plymouth, PL4 8AA,
United Kingdom

²British Geological Survey, Natural Environment Research Council, Environmental Science Centre,
Keyworth, Nottingham, NG12 5GG, United Kingdom

³COMET, School of Earth and Environment, University of Leeds, Leeds LS2 9JT, UK

Key Points:

- Studying N-S motions from InSAR in western Türkiye highlights key factors for successful inversion are fast deformation rates and low noise
- Vertical InSAR velocity field reveals shifts from uplift to subsidence spatially correlated with faults and fault splays
- Results indicate spatial variation in uplift rates along faults and could be used to infer the relative activity of faults or fault splays

Abstract

Quantifying interseismic deformation of fault networks which are predominantly deforming in a north-south direction is challenging, because GNSS networks are usually not dense enough to resolve deformation at the level of individual faults. The alternative, synthetic aperture radar interferometry (InSAR), provides high spatial resolution but is limited by a low sensitivity to N-S motion. We study the active normal fault network of Western Anatolia, which is undergoing rapid N-S extension, using InSAR. In the first part of this study, we develop a workflow to assess the potential of decomposing InSAR line-of-sight (LOS) velocities to determine the N-S component. We use synthetic tests to quantify the impact of noise and other velocity components and outline the requirements to detect N-S deformation in future studies. In its current state, the N-S deformation field is too noisy to allow robust interpretations, hence in the second part we complement the study by including vertical deformation. Since most faults in the study region are normal faults, the high-resolution vertical velocity field provides new insights into regional active faulting. We show that tectonic deformation in the large graben systems is not restricted to the main faults, and seemingly less active or inactive faults could be accommodating strain. We also observe a potential correlation between recent seismicity and active surface deformation. Furthermore, we find that active fault splays causing significant surface deformation can form several kilometres away from the mapped fault trace, and provide an estimate of current activity for many faults in the region.

1 Introduction

1.1 Can we Extract North-South Deformation from InSAR?

Fialko et al. (2001) and Wright et al. (2004) first described the process of decomposing interferometric synthetic aperture radar (InSAR) line-of-sight (LOS) signals into east-west, north-south and vertical components. Today, with the availability of high performance computing, InSAR time series, and improved satellite systems (namely the Sentinel-1 system), this process has become a well-established application. Nevertheless, one particular challenge is the accurate quantification of N-S deformation, due to the inherently poor InSAR sensitivity to movements in direction of the satellite's orbit (Wright et al., 2004). Since the Sentinel-1 satellites (similar to previous SAR missions) are on approximately N-S-oriented orbits, the LOS velocity is significantly less sensitive to north-south deformation compared to movements in the vertical and east-west directions. Other studies solved the north component either by assuming it to be negligible (Hussain et al., 2016) or performing a joint inversion of InSAR LOS velocities while constraining the north component using spatially smoothed GNSS velocities (Samsonov et al., 2008; Vollrath et al., 2017; Hussain et al., 2018; Weiss et al., 2020), or by including other techniques, such as azimuth offset tracking (Fialko et al., 2001; Hu et al., 2014). Despite these efforts, determining N-S deformation remains difficult. This is a critical problem for regions that predominantly deform in the N-S direction, since the real deformation is drastically underestimated by LOS velocity maps. One such example is the Western Anatolian Extensional Province (WAEP) in south-west Türkiye. GNSS studies show that the region is undergoing rapid N-S extension of ~ 20 mm/yr (Aktug et al., 2009; McClusky et al., 2000) across a series of graben structures (McKenzie, 1972; Ten Veen et al., 2009) that have hosted large infrequent earthquakes $\leq M_W 7.0$ (Eyidoğan & Jackson, 1985). The current state of activity on the graben fault systems is still not fully understood and so investigations into the regional fault network and deformation patterns can contribute to an understanding of fault activity and therefore seismic hazard.

Here we use an alternative approach to determine the north-south component of deformation, by constraining the E-W component with GNSS velocities and using an over-determined inversion of InSAR time series LOS data. Our technique makes use of the deviation of the Sentinel-1 orbits from north. The study area in SW Türkiye features

rapid N-S extension, a set of well-studied fault zones, and a dense GNSS network allowing the method to be tested in this region.

In the first part of this study, we explore the capabilities and limitations of detecting N-S surface deformation using InSAR-derived deformation maps. We use synthetic tests to determine general methodological constraints and possibilities to yield robust interpretations from inverted N-S velocity fields. We outline the requirements to successfully extract N-S deformation, and show the impact of deformation in other directions when decomposing LOS velocities. Using these insights, we apply the same process to real data, trying to infer north-south velocities in SW Türkiye at resolution of individual faults.

1.2 Vertical Deformation of Active Normal Faults

The N-S deformation in western Anatolia is mostly accommodated by \sim E-W trending normal faults (Bozkurt & Sözbilir, 2004; Ten Veen et al., 2009). Since the extraction of reliable N-S deformation is challenging, we complement our analysis of the active faults with vertical deformation rates. However, while InSAR is highly sensitive to vertical movements, this comes with a different challenge; the studied faults are mainly graben-bounding faults, separating flat, sediment-filled basins covered by agricultural land from mountainous areas. Consequently, the effects of topography, atmosphere and subsidence, owing to ground water extraction in the grabens, swamp the tectonic signal and complicate the ability to quantify or even detect tectonic subsidence (Hastaoglu et al., 2023; Aslan et al., 2022; Imamoglu et al., 2022). Therefore, the key challenge is to distinguish tectonic movements from other confounding influences. We navigate this problem by focusing on the footwall uplift of normal faults and neglecting the hangingwall deformation. While subsidence in the basin (hangingwall of normal faults) can have a variety of causes, footwall uplift can be mainly attributed to tectonic factors.

We quantify footwall uplift rates along active faults in the region and compare the spatial uplift patterns with the mapped fault traces. This provides insights into the activity of individual faults and fault plays, which are not detectable with other techniques.

2 Surface Deformation in the Western Anatolian Extensional Province

2.1 Regional Tectonics and Seismic Activity

Driven by the collision of the African, Eurasian and Arabian plates, the Anatolian microplate escapes westward between the North Anatolian (NAFZ) and East Anatolian (EAFZ) Fault Zones at a rate of 20-30 mm/year (Kurt et al., 2023). Owing to this movement, combined with roll back from the Hellenic Arc subduction zone, western Anatolia and parts of the Aegean Sea are undergoing N-S extension at rates of ~ 20 mm / year, forming the Western Anatolian Extension Province (Aktug et al., 2009; McClusky et al., 2000; McKenzie, 1978, 1972; Jackson, 1994; Taymaz et al., 2007). The dominant style of deformation in the WAEP is normal faulting on \sim E-W-trending faults, forming a series of elongated basins (grabens). In the eastern Aegean Sea and coastal regions of Anatolia, often referred to as the 'İzmir-Balıkesir transfer zone', a significant right-lateral component of deformation is expressed in active strike-slip deformation on \sim NE-SW-trending faults (Uzel et al., 2012).

The most prominent structures in the study area are the E-W-trending Gediz and Büyük Menderes Graben, the Simav Graben in the north and the Gulf of Gökova at the Mediterranean coast (Fig. 1). Other basins, predominantly bounded by active, NW-SE or NE-SW-trending normal faults, are distributed across the WAEP. For our study we use a simplified fault network modified from the active fault database (Emre et al., 2018) and the accompanying active fault map series (1:250k scale). Faults in the Denizli basin after Koçyiğit (2005), Çameli region after Alçiçek et al. (2006) and Yang et al. (2020).

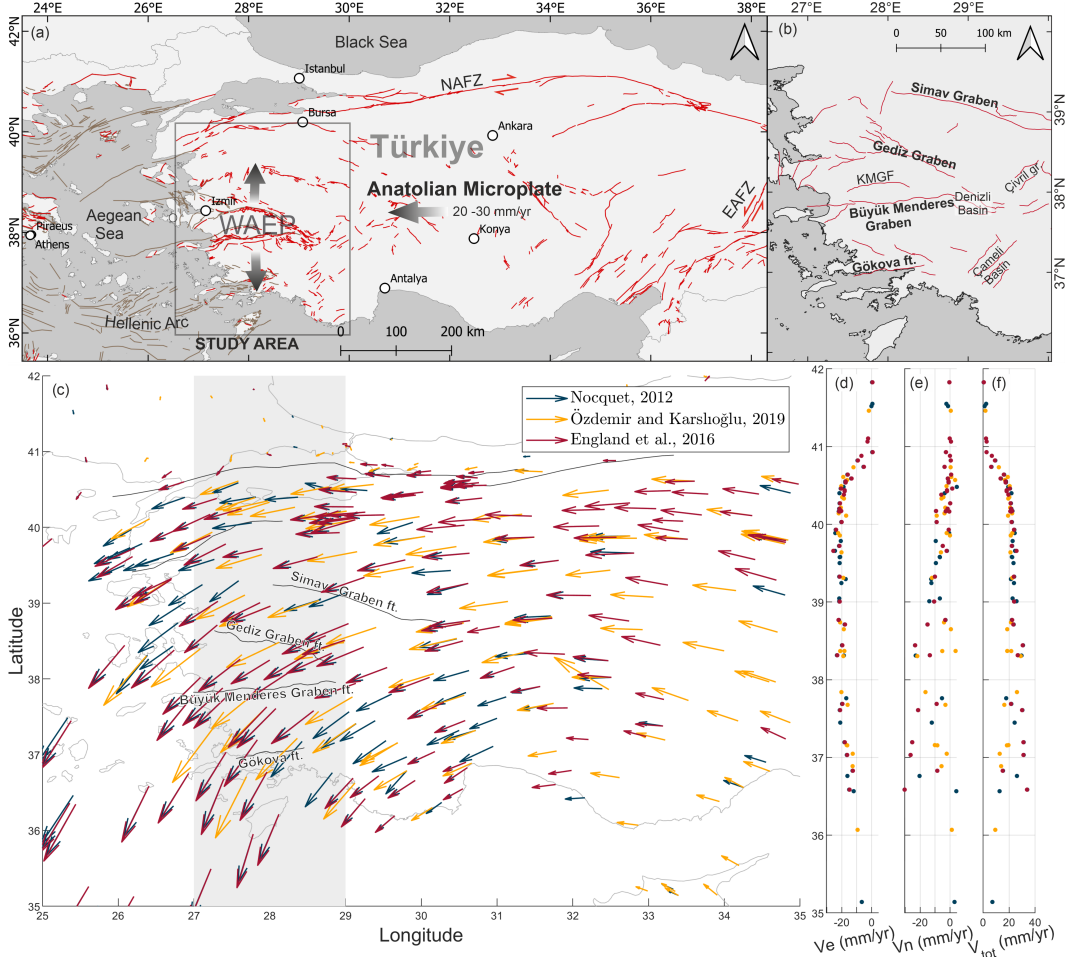


Figure 1. a) Tectonic setting and major active fault zones of the Eastern Mediterranean (after Emre et al. (2018); Ganas et al. (2013, 2023)). Box indicates the extent of the study area. NAFZ: North Anatolian Fault Zone; EAFZ: East Anatolian Fault Zone b) Simplified fault network of the Western Anatolian Extensional Province (WAEP); KMGF: Küçük Menderes Graben Fault. c) GNSS velocity field of Türkiye. Grey-shaded area marks the profile depicted in d, e, and f. GNSS velocities relative to stable Eurasia, hence the increase in both E-W and N-S components with distance to the NAFZ.

Table 1. Sentinel-1 frames, time span covered, and number of interferograms (n ifgs) used to calculate time series.

frame ID	geometry	start date	end date	n ifgs
036D_04976	descending	13/03/2015	30/01/2023	1258
036D_05175	descending	08/10/2014	28/06/2022	1003
138D_04954	descending	15/10/2014	29/07/2022	1173
138D_05142	descending	15/10/2014	13/01/2023	1498
138D_05325	descending	08/11/2014	29/07/2022	1147
058A_04914	ascending	09/01/2014	19/01/2023	1358
058A_05086	ascending	09/10/2014	27/08/2021	916
058A_05279	ascending	09/01/2014	09/09/2022	1293
131A_04951	ascending	02/01/2018	31/12/2022	1004
131A_05153	ascending	07/11/2014	28/07/2022	1053
131A_05336	ascending	07/11/2014	31/12/2022	1165

Fault traces were simplified to single lines and the location of the fault traces was modified based on morphology (DEM) and vertical deformation signals, where applicable.

2.2 Tectonic and Non-Tectonic Surface Deformation

Hooper et al. (2012) and Weiss et al. (2020) computed the InSAR line-of-sight (LOS) velocity fields throughout Anatolia. Weiss et al. (2020) decomposed LOS velocities of entire Türkiye into east-, north- and vertical components, though the north component was constrained by smoothed, interpolated GNSS velocities.

Surface deformation and aseismic creep is documented in several locations in the WAEP, for example in the Afyon-Akşehir Graben (Özkaymak et al., 2019). Particularly fast deformation rates are observed at the Sarigöl fault, the eastern segment of the Gediz Graben system, which ruptured in the 1969 M_W 6.9 Alaçehir earthquake (Arpat & Bingöl, 1969; Eyidoğan & Jackson, 1985). Vertical deformation at the fault was 70–87 mm/yr between July 2017 and 2020, inferred from precise levelling studies (Doğan et al., 2022). Other studies obtained vertical deformation of 60–85 mm/yr over a 10-year period (Koca et al., 2011) or up to 90 mm/yr (Poyraz et al., 2019).

Most of the surface deformation observed is owing to subsidence in the grabens related to falling ground water levels, particularly in the summer. Since minor deformation continues throughout winter and spring, Doğan et al. (2022) conclude that tectonic creep also contributes to the observed vertical deformation, possibly in a range of ~ 20 mm/yr. When removing the seasonal signal, which is mainly caused by groundwater level changes, from the time series, Hastaoglu et al. (2023) determined between 10 and 62 mm/yr of subsidence in the graben. Subsidence related to ground water level changes is known from multiple basins across the region (Aslan et al., 2022; Imamoglu et al., 2022). It generally exceeds tectonic deformation rates and is difficult to deconvolute from the tectonic subsidence. Therefore, we focus our analyses on the uplift signal of normal faults.

3 Methods

3.1 Preparing InSAR and GNSS Velocities

We computed InSAR time series of six ascending and five descending frames (Table 1, Supplement 3) using LiCSBAS (Morishita et al., 2020) with data downloaded from the LiCSAR portal (Lazecký et al., 2020). This analysis included atmospheric corrections using GACOS data (Yu et al., 2018). Following the approach of Hussain et al. (2016), the InSAR LOS velocities are referenced to a stable Eurasia reference frame, using three

sets of GNSS velocity data (Nocquet, 2012; England et al., 2016; Özdemir & Karshoğlu, 2019). We combine the data, averaging values for duplicate stations, and calculate the average InSAR LOS velocity in a square of $\sim 1 \text{ km}^2$ around each GNSS station. GNSS north (V_n) and east (V_e) velocities are converted into LOS velocities using the InSAR LOS vector components (p_x and p_y) for the east and north directions, assuming that proportions of InSAR velocities are comparable to GNSS velocities: $LOS_{gnss} = p_x \times V_e + p_y \times V_n$. We then determine the best-fit planes through the InSAR and GNSS LOS velocities. The difference between both planes reflects the difference of reference frames between the GNSS (relative to stable Eurasia) and the InSAR velocities, and is subsequently removed from the InSAR LOS velocity field. The procedure is repeated for each InSAR frame.

To use multiple InSAR data sets, combined with GNSS velocities, they must be on the same geographic grid. We therefore create a grid covering the study area from 26 to 31°E and 36 to 40.5°N, with a grid size of 0.0045° (500 m). We interpolate the GNSS velocities onto this grid, and then resample all InSAR LOS velocities on the grid, using the nearest-neighbor method and preserving empty pixels.

The LOS velocities differ slightly between frames, even for frames on the same track. These differences result in artificial steps at frame boundaries in the combined velocity fields and later inversion results, and could mislead interpretations when falsely identified as natural features in the surface deformation rates. To reduce these artifacts, we apply another correction step, without changing the relative signals within each frame. For each geometry, one reference frame is picked (descending 138D 05142 and ascending 131A 05153), which is located in the centre of the study area and shows reasonably good time series results. The secondary frame with the largest overlap area (omitting empty pixels) with the reference frame is determined. To adjust the velocity field to a similar range in velocities, the secondary frame (LOS_{sec}) is corrected by the standard deviation σ of the overlapping parts of the reference frame: $LOS_{sec}^{adj} = LOS_{sec} \times \sigma_{ref} / \sigma_{sec}$. Then the median of velocities of both frames in the overlapping area is determined and the reference frame is corrected: $LOS_{sec}^{adj} = LOS_{sec} + m_{ref} - m_{sec}$, where m_{ref}, m_{sec} is the median of the reference/secondary LOS velocities, respectively, in the overlapping area. This process is repeated for all frames, each time the reference area is enlarged by the newly referenced frame. Before the inversion, all frames are merged on the same track into single data sets (two ascending and two descending tracks), averaging overlapping pixels.

3.2 Inversion of the InSAR North Component

The line of sight (LOS) velocity can be decomposed into the three components of displacement, D_E , D_N , and D_U , by

$$D_{LOS} = \begin{bmatrix} \sin(\theta)\cos(\alpha) & -\sin(\theta)\sin(\alpha) & -\cos(\theta) \end{bmatrix} \begin{bmatrix} D_E \\ D_N \\ D_U \end{bmatrix} \quad (1)$$

The row vector is defined by the incidence angle θ and the azimuth of the satellite track α (Wright et al., 2004). It specifies the components of the vector $\hat{p} = (p_x, p_y, p_z)$ pointing from a point on the ground to the satellite and thus determining the proportions of eastward, northward and vertical displacement in the LOS velocity. Similarly, the LOS displacement of each point can be defined by

$$D_{LOS} = p_x D_E + p_y D_N + p_z D_U \quad (2)$$

Since equations 1 and 2 contain three unknowns, at least three data sets are required to solve for the displacement vector \hat{D} containing the east (D_E), north (D_N), and vertical (D_U) components of displacement. Since the eastward velocities are well constrained by GNSS data, we assume that $D_E = GNSS_{east}$ and subsequently constrain the E-

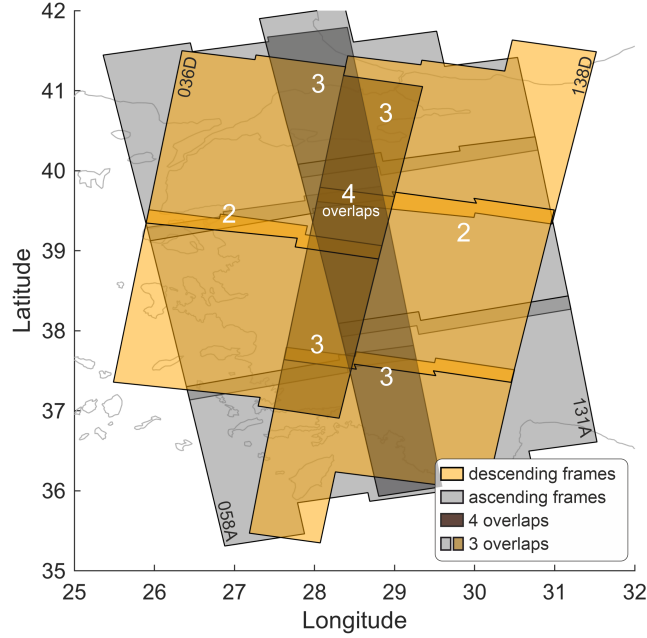


Figure 2. Overlapping areas of the five descending and six ascending Sentinel-1 frames covering the study area. The central region is covered by four overlapping tracks.

W component by a smoothed interpolated GNSS velocity field. The study area is covered by Sentinel-1 ascending tracks 058 and 131 and descending tracks 036 and 138 (Fig. 2). For each pixel, data from at least two overlapping frames are available and the centre of the study region is covered by up to four overlapping frames. Therefore, for the central part of the study area we have an over-determined system with up to five data sets ($4 \times \text{InSAR}$ and $1 \times \text{GNSS}$) but still only three components to solve for. A least squares inversion is used to solve for \hat{D} , following the general equation

$$\begin{bmatrix} LOS_D^{036} \\ LOS_D^{138} \\ LOS_A^{131} \\ LOS_A^{058} \\ GNSS_{east} \end{bmatrix} = \begin{bmatrix} p_x^{036} & p_y^{036} & p_z^{036} \\ p_x^{138} & p_y^{138} & p_z^{138} \\ p_x^{131} & p_y^{131} & p_z^{131} \\ p_x^{058} & p_y^{058} & p_z^{058} \\ 1 & 0 & 0 \end{bmatrix} \times \begin{bmatrix} D_E \\ D_N \\ D_U \end{bmatrix} \quad (3)$$

The number of InSAR data sets in the matrix varies between two and four, using the maximum of available look angles for each pixel. The east component p_x is constrained with GNSS velocities, thus D_E is effectively removed from the system. Although the inversion is theoretically solvable with only two LOS velocities, the resulting north-component is highly erroneous and noisy, likely owing to the poor north-sensitivity. To account for this issue, only pixels covered by at least three InSAR tracks are included, thus using an over-determined system. This increases the robustness of the inversion results, but at the expense of spatial coverage, since areas only covered by two overlapping frames are now excluded. Since we work with displacement velocities, in the following we will refer to the E-W, N-S, and vertical components of deformation as V_e , V_n , and V_u , respectively.

3.3 Synthetic Data Tests

Tests with synthetic velocities are used to simulate inversion with known north-south and vertical velocities, to determine if these are identifiable after converting into

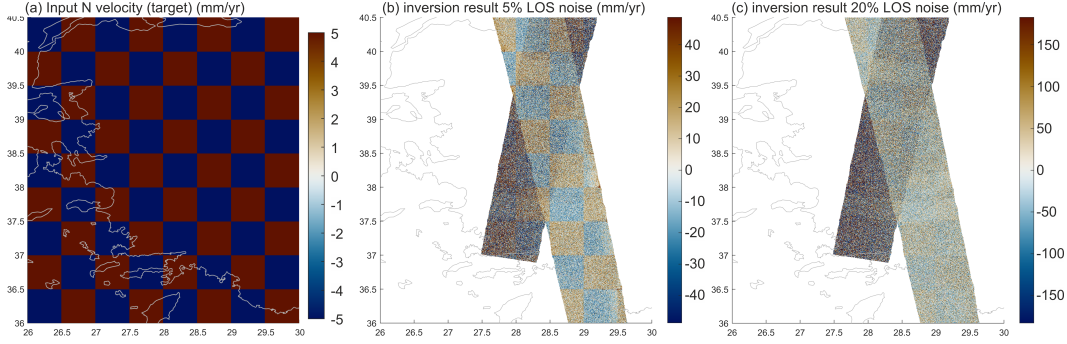


Figure 3. Test with synthetic checkerboard pattern velocity fields. a) Input N-S velocity field with alternating $V_n = \pm 5$ mm/yr. We combined the velocity components to the LOS and added random noise between 0 and 20% of the LOS velocity. b) and c) show the results of the inversion solving for V_n . The checkerboard pattern is clearly visible for 5% noise, but unclear by noise at 20%. This gives approximate input data quality boundaries for inversion of real N-S velocities.

LOS velocities and decomposing back into the three components. For the north component a checkerboard pattern is used, each square with a size of $0.5^\circ \times 0.5^\circ$ and velocities of $+5$ and -5 mm/yr (Fig. 3). The east component is defined by a ramp signal increasing from -10 in the west to -20 mm/yr in the east of the study area, which is similar to the real westward motion of Western Anatolia (Kurt et al., 2023). The vertical velocities are kept constant across the study region; vertical velocities are varied between -1 and -10 mm/yr to test the impact on the inverted N-velocities.

Synthetic components are converted into LOS velocities using Equation 2 and the look vector components p_x , p_y , and p_z for each frame. To simulate noise of the radar acquisition, for example from residual atmosphere, normally distributed noise is added to the LOS data. Noise is varied between 0 and 25% of the maximum LOS velocity to test its impact on the inverted N-S velocity (Figure 3). The synthetic InSAR frames have the same look vectors and spatial extent as real data. A series of tests with variable noise in the LOS input is performed and the goodness of the inversion is quantified with the root mean square error (RMSE) to compare areas covered by 3 vs 4 tracks, and the impacts of varying V_u and V_n input velocities on the inverted V_n (Fig. 4). As input noise introduces a random component, all tests were repeated three times and outputs averaged to ensure reliable results.

Additionally, the impact of the V_n and V_u components on the inversion is assessed, again simulating these with a checkerboard pattern of alternating ± 5 mm/yr velocities. Varying one component at a time, the mean inverted velocity in the positive and negative checkerboard squares is determined (Fig. 5), and compared to the input velocity (± 5 mm/yr).

3.4 Inversion of Vertical Velocities

Inversion of the vertical velocity field follows the same routine as solving for the N-S component, with the difference that Equation 3 is solved for V_e and V_u , and V_n is constrained with the GNSS velocity field. The vertical velocity is computed for the entire study area, with a pixel resolution of 100m.

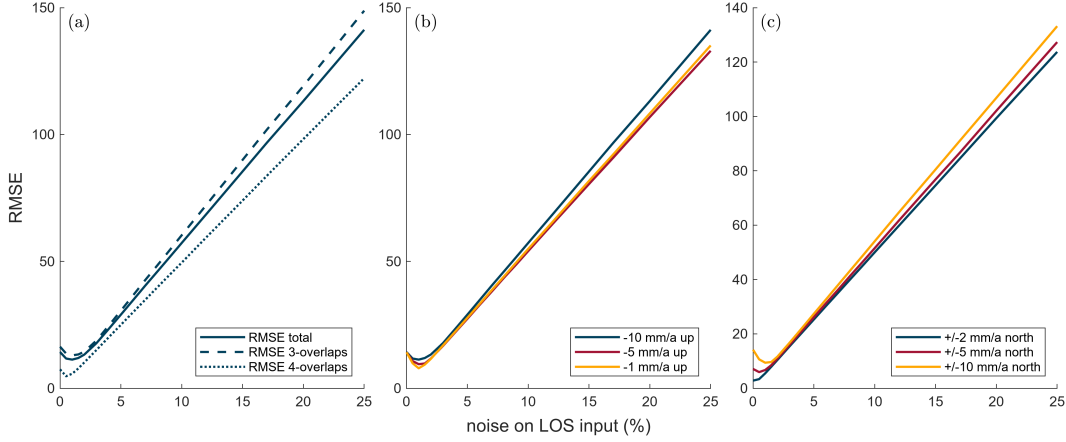


Figure 4. Noise in input velocities vs. root mean square error (RMSE) comparing synthetic (checkerboard) N-S velocities and inversion results. a) Comparison between regions covered by 4 vs 3 overlapping Sentinel-1 tracks, showing improved RMSE in the 4-overlap zone (constant $V_u = -10$ mm/yr). b) Varying the vertical velocity component (V_u) has a negligible effect on the inverted V_n . c) Varying north-south velocities (V_n) (with a fixed $V_u = -0.5$ mm/yr) also has a negligible impact

4 Results

4.1 Synthetic Tests

Tests with synthetic velocity fields are performed to quantify the impact of noise and different velocity components on the inverted N-S and vertical deformation field (Fig. 4). All tests show a linear relationship between noise in the LOS data and RMSE, and errors are significantly reduced in areas covered by four overlapping frames (Fig. 4a). Rapid subsidence can have a minor impact on RMSE (Fig. 4 b). Surprisingly in the tests, increasing N-S deformation yields a slightly increased RMSE (Fig. 4c). Additionally the input N-S and vertical deformation fields (checkerboard pattern) are compared to the inverted deformation (Fig. 5). V_n is increased both in positive and negative squares, across the entire range of tested V_u , with constant V_e gradient of -10 to -20 mm/yr. Similarly, inverted V_n are shifted towards negative values at a constant subsidence of 5 mm/yr and varying V_e (Fig. 5a). The inverted vertical deformation (V_u) is generally much closer to the target velocity of ± 5 mm/yr and RMSE is usually < 2 mm/yr. V_u is generally underestimated independent of V_n input, with clear correlation between V_e and the inverted V_u (Fig. 5b). Impact of the other components on the inversion results increases with noise.

4.2 North-South Deformation

The resulting N-S velocity field indicates that the majority of velocities (within 3σ) are in a range of ± 448 mm/yr (Fig. 6), exceeding realistic values. Notable differences in N-S velocities are observable between areas covered by different tracks. The central-northern region of the study area, which is covered by four overlapping tracks, has the lowest standard deviations. This area also shows the most consistent and realistic velocities, mostly in a range of $< \pm 50$ mm/yr.

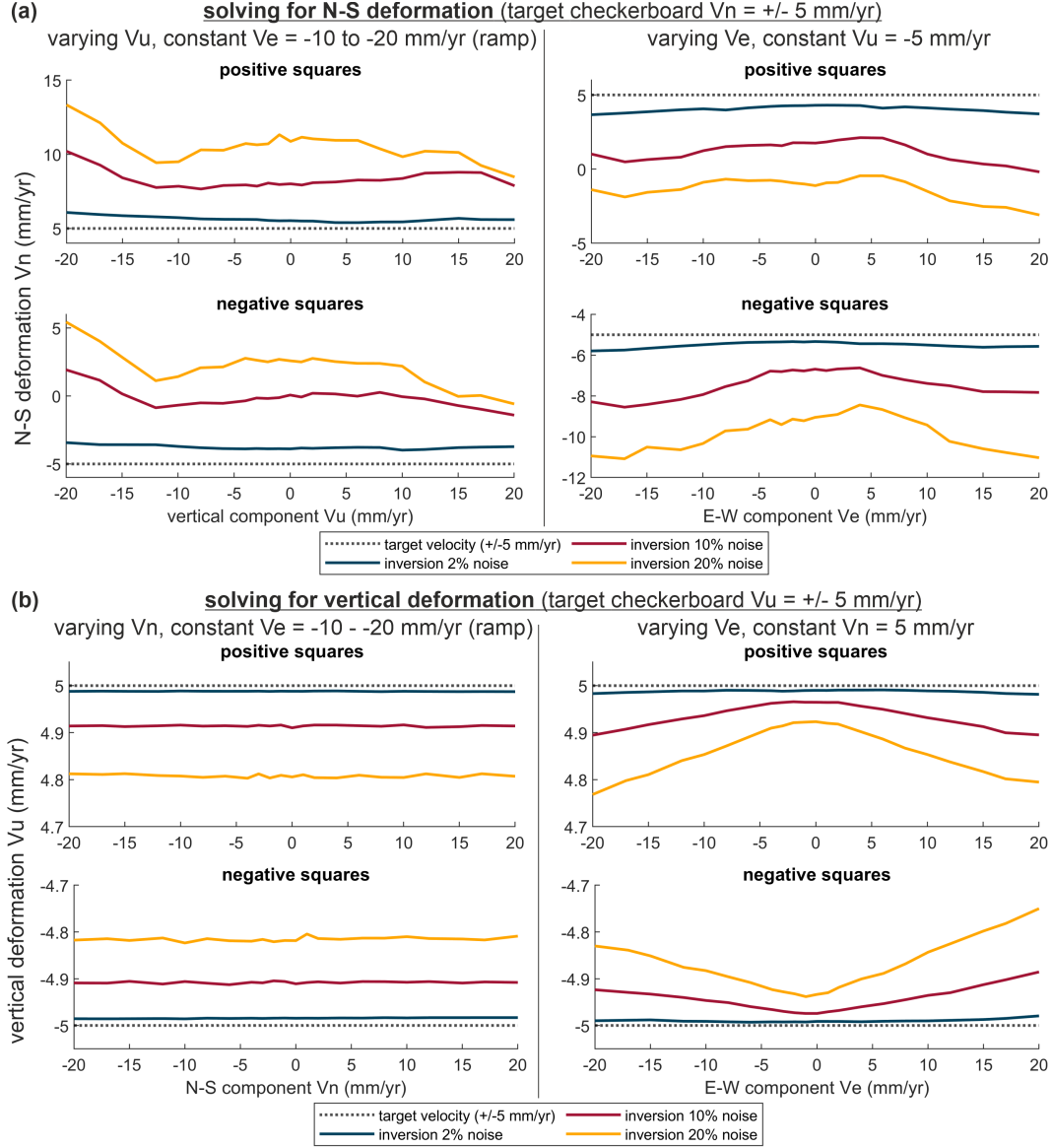


Figure 5. Impact of other components on the inversion results, tested with synthetic data. a) Inversion for N-S velocities. V_n is shifted towards positive velocities for all V_u (left), indicating that another factor, probably the rapid V_e , causes a general shift of the inverted V_n . Similarly, V_n is shifted towards negative values for all V_e (right), implying impact of the constant V_u on the V_n inversion results. In short: westward motion leads to false northward motion in inversion, whereas subsidence leads to southward trends. b) Inversion for vertical velocities, generally showing much less deviation from the target (input) velocity (V_u). V_u is decreased for both positive (uplift) and negative (subsidence) areas, across all tested V_n values, implying a general influence of the E-W component. The right plots confirm this, showing that V_u tends to decrease with increasing V_e , though deviations from the input velocity are ≤ 0.25 mm/yr.

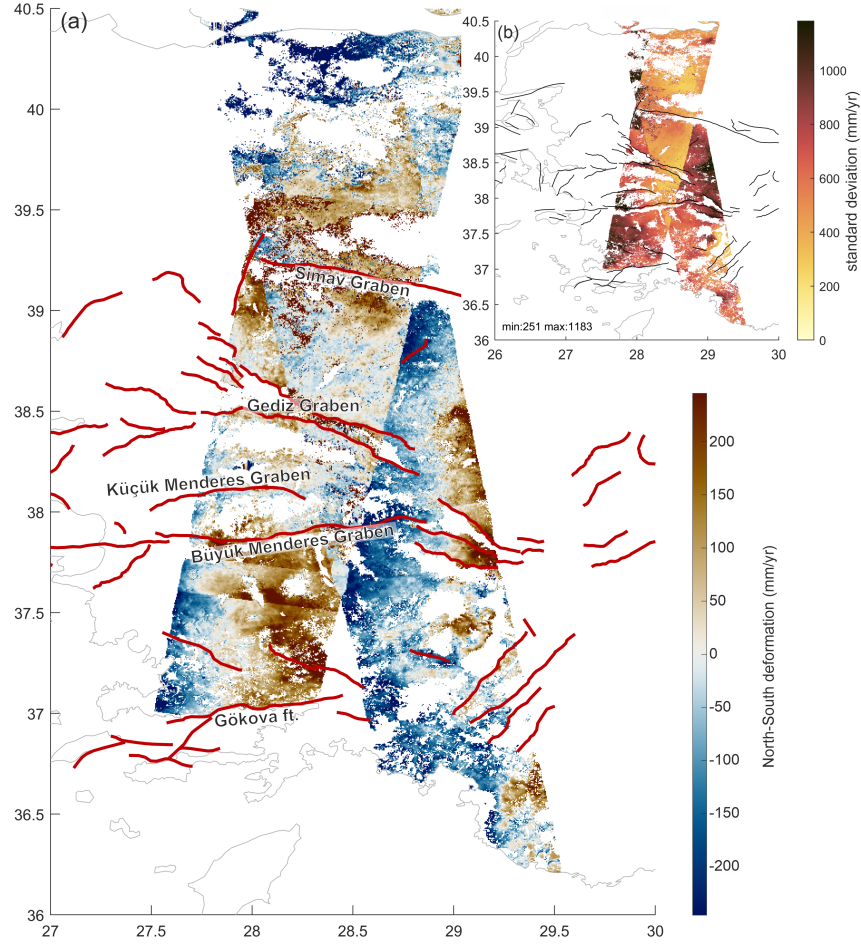


Figure 6. N-S velocity field of SW Türkiye (a) and standard deviations (b). Deformation exceeds realistic rates, and the velocity field shows artefacts at frame boundaries. Red lines depict active faults.

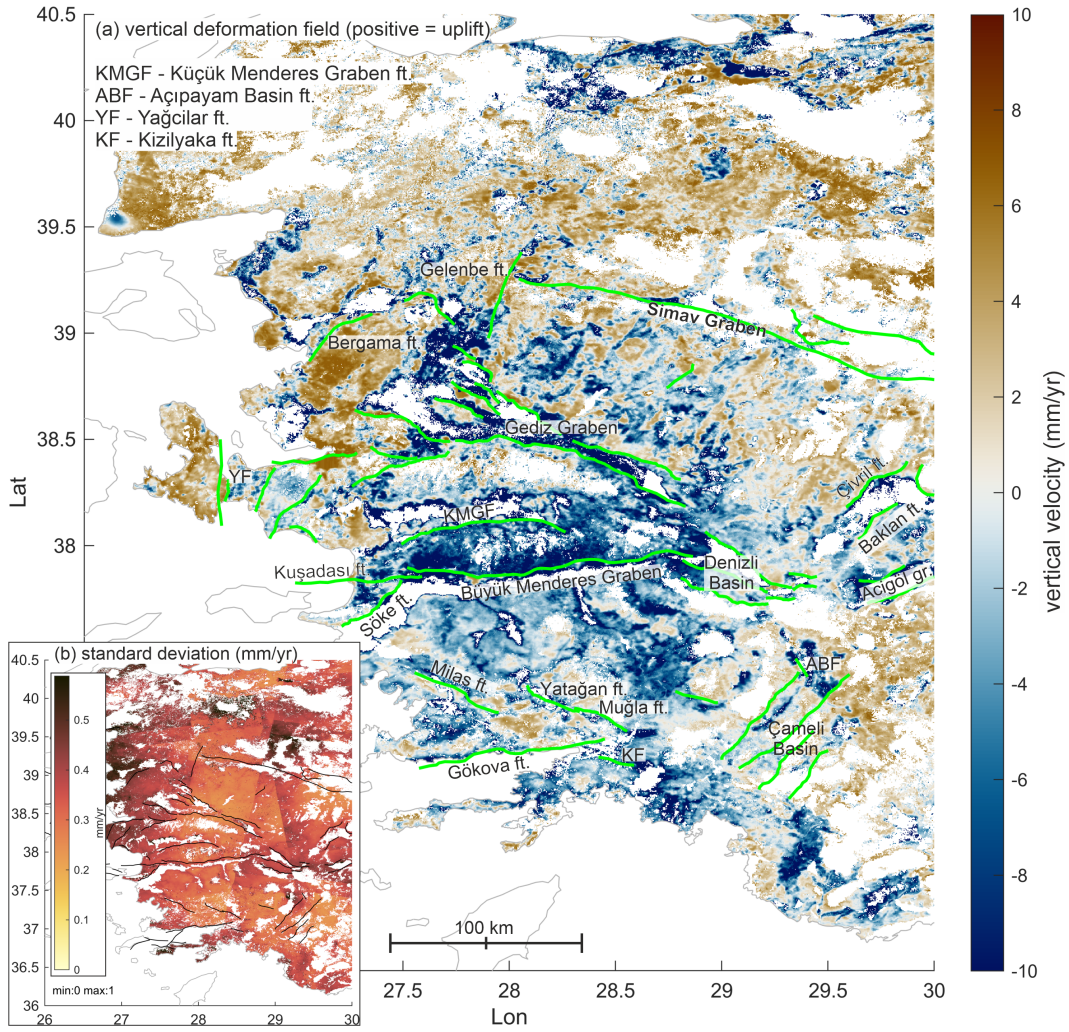


Figure 7. a) Vertical velocity field and simplified fault network (green lines). b) standard deviation

Table 2. Footwall uplift rates of faults with clear tectonic uplift signal, determined from across-fault swath profiles. Maximum is the fastest uplift rate of all profiles, mean is the average of maximum velocities from all profiles. See Figures 7 and 8 for fault locations.

Fault	mean (mm/yr)	max. (mm/yr)	comments
Killik ft.	1.83	6.24	
Kemerdaamlari ft.	3.43	6.38	
Halitpaşa ft.	1.82	4.21	
Ozanca ft.	2.87	6.01	
Gölmarmara ft.	-2.99	2.72	only eastern segment shows deformation
Akselendi ft.	3.73	5.35	
Akhisar ft.	2.10	5.20	
Pamukkale ft.	0.34	2.68	Denizli basin
Honaz ft.	0.97	2.39	
Aşağıdağdere ft.	0.16	1.48	
Kaleköy ft.	-0.33	1.92	naming adapted from Koçyiğit (2005)
Söke ft.	3.82	1.19	
Milas ft.	1.38	3.44	only western segment shows clear deformation
Gökova ft.	1.54	4.60	
Çivril ft.	2.29	4.01	
Baklan ft.	1.65	3.60	
S Acigöl Graben ft.	2.66	4.35	
N Acigöl Graben ft.	-2.15	1.57	
Acıpayam Basın ft.	2.13	3.99	2019 M_W 5.8 source (Yang et al., 2020)
Yağcılar ft.	5.09	6.19	

4.3 Vertical Deformation and Relative Fault Activity

4.3.1 Regional trends

The vertical deformation field broadly shows uplift in the northern parts of the study area, whereas the central and southern region, especially the region around the Büyük Menderes Graben, are dominated by subsidence of up to -12 mm/yr (Fig. 7).

Several, but not all active faults show a difference in vertical deformation across mapped fault traces, with uplift in the footwall and subsidence in the hangingwall. The fastest deformation is observable at fault zones in the Gediz Graben. Other faults showing active deformation are, for example, the Pamukkale fault in the Denizli basin, the Çivril, Baklan and Acigöl graben faults in the north-east and the Gökova and Söke faults in the south. Uplift rates were determined for all faults that show a clear tectonic deformation signal approximately along the mapped fault traces (Table 2). Faults with unclear or weak uplift signal are, for example, the Muğla, Yatağan, Babdağ and Kuşadası faults. Faults in the İzmir region, which have a notable strike-slip component, mostly show very little vertical deformation (with the exception of the Yağcılar ft.) similar to faults in the Çameli basin. We also investigated several faults with uncertain Holocene activity, the Gelenbe fault north of the Gediz Graben and the Kızılyaka fault east of the Gulf of Gökova, which unsurprisingly show no surface deformation. In contrast, the Küçük Menderes Graben features notable uplift along the northern margin, where no active fault is known to date, as well as a weak signal at the southern margin, which likely hosts the Küçük Menderes Graben Fault (KMGF), though its recent activity is not clear (Seyitoğlu & Işık, 2009). Several faults which are clearly active, such as the BMGF, show very slow active surface deformation. Note that uplift rates can be influenced by regional uplift or subsidence and thus are not directly convertible to fault throw/slip rates.

4.3.2 Notable Characteristics of Active Deformation in the Gediz Graben

The dominant tectonic structure of the Gediz (Alaşehir) Graben is the detachment fault at the southern side, which has been active since Miocene, exhuming the Menderes Massif. It forms a low-angle detachment dipping $\sim 15\text{--}30^\circ$ to the north and is believed to be inactive, while the active high-angle Gediz Graben Bounding Fault (GGBF) formed in its hangingwall (Gessner et al., 2001; Seyitoğlu et al., 2002; Bozkurt & Sözbilir, 2004; Purvis & Robertson, 2004; Çiftçi & Bozkurt, 2009). The GGBF consists of three segments, the eastern Alaşehir segment, the central Sahlili segment and the western Turgutlu/Armutlu segment. Naming and mapped fault traces, especially for the western segment and adjacent faults, vary in literature. Kent et al. (2016) used cross-sections interpreted from published seismic and outcrop maps and the relationship between throw and relief to determine the long-term slip rates along the GGBF. Throw rates (vertical part of slip rates), are in the range of $0.4 - 1.3$ mm/yr (Kent et al., 2016), accelerating to up to 2.0 mm/yr at about $0.6\text{--}1$ Ma (Kent et al., 2017). The northern side of the graben hosts the antithetic Killik and Kemeramları Faults. In the west, the graben splits up into several sub-basins hosting multiple active faults.

Almost all mapped faults in the graben show a clear deformation signal. We quantify deformation using 1 km wide swath profiles across the fault traces, perpendicular to the mean fault strike (see Fig. 8c). For robust quantification of the maximum uplift, we first take the average of all values along the profile (red line), then we determine the maximum of this within the footwall (dark grey) of the profile. The maximum value (grey shaded) of the red curve and the spread of values at this point are used to create along-fault uplift profiles (Fig. 8d&e). Assuming that the slip distribution of the observed tectonic deformation is comparable to long-term fault slip, a triangular, or elliptical slip distribution would be expected, with the maximum slip in the fault centre, decreasing towards the tips (Cowie & Roberts, 2001; Manzocchi et al., 2006; Roberts, 2007; Schlagenhauf et al., 2008).

The vertical deformation field can be used to infer relative fault activity (see Section 5.3.3). Furthermore, detailed analyses reveal insights into several commonly misinterpreted characteristics of regional faulting; Firstly, vertical deformation is not focused on the southern side of the graben, which hosts the main graben bounding fault. While all faults in the graben show vertical deformation, the antithetic faults in the north (Kemeramları and Killik Ft.) in some parts appear to be moving faster than the GGBF. In the graben centre, the Halitpaşa and Ozanca faults are uplifting and tilting smaller blocks at $\sim 3\text{--}5$ mm/yr (Fig. 8b). Secondly, the southern graben margin shows two deformation fronts (Fig. 8c). These correlate with the locations of the active GGBF in the north and the low-angle detachment fault in the south, suggesting that the Gediz detachment, contrary to established opinions (Gessner et al., 2001; Seyitoğlu et al., 2002), might still be active. Thirdly, deformation at the GGBF (Fig. 8d) is faster on the western and central segments with up to ~ 6 mm/yr uplift, but comparably slow on the eastern (Alaşehir) segment, which ruptured in a M_W 6.9 earthquake in 1969 (Eyidoğan & Jackson, 1985; Arpat & Bingöl, 1969).

Finally, the Manisa Ft. shows a fast uplift of $\sim 5\text{--}7$ mm/yr along most of its length, exceeding long-term slip rates based on ^{36}Cl -dating (Mozafari et al., 2022). The eastern part of the mapped fault, connecting to the GGBF, shows no active deformation. Noticeably, the mapped fault trace and morphologic scarp and the active deformation front mismatch by up to ~ 6 km in the western part of the fault (Fig. 8e & f).

5 Interpretation and Discussion

5.1 Insights from Synthetic Data Tests

The main factor determining the accuracy of N-S inversion is noise in the LOS velocity. Synthetic tests show that the noise in LOS data must be approximately $\leq 5\%$ to reasonably invert for the N-S component. Although noise in real LOS velocities is dif-

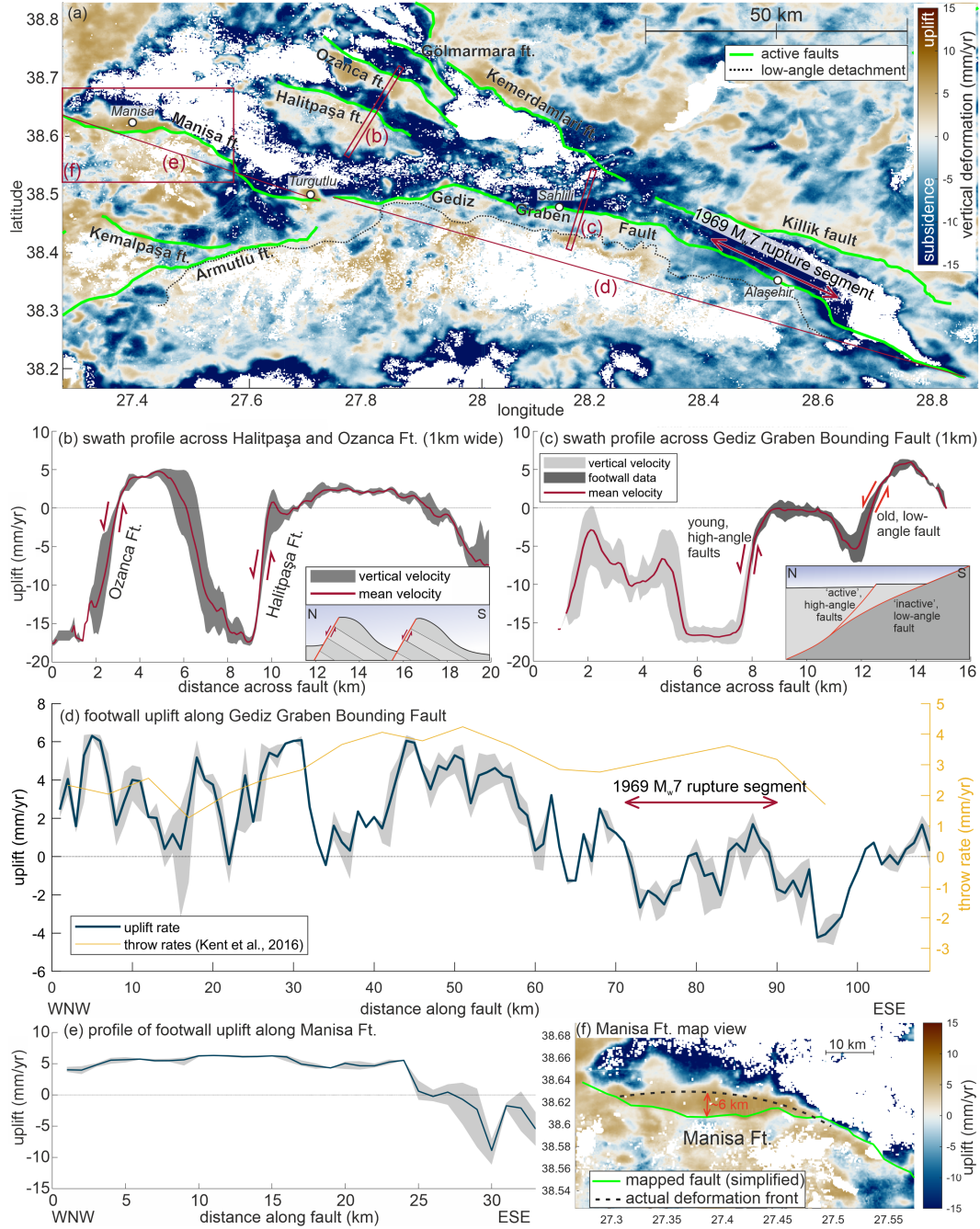


Figure 8. Vertical deformation in the Gediz Graben. (a) Vertical deformation field and mapped faults (simplified). Red boxes outline swath profiles b and c, and map f, red lines indicate the along fault profiles d and e. (b) Swath profile across the Halitpaşa and Ozanca Ft., showing clear uplift; inset depicts cartoon of block tilt. (c) Swath profile across the GGBF, showing deformation at both the old, low angle, and the young, high angle fault splays. (d) Along-strike profile of the GGBF footwall, from 109 across-fault swath profiles. Note the contrast in uplift rates between the 1969 rupture segment and the central/western part of the fault. Throw rates from river profiles (Kent et al., 2016) vary between 1.3 and 4.2 mm/yr, with the fastest rates in the centre of the fault. (e) Along-strike profile of the Manisa Ft. footwall, from 34 swath profiles (f) Map view of the Manisa Ft., the mapped fault trace and the current deformation front are up to ~6 km apart.

difficult to quantify, this shows that solving for V_n is theoretically possible if the signal / noise ratio can be improved. Although two data sets are mathematically sufficient to solve the regression (with one component constrained by GNSS data), we found that only an overdetermined system with at least three LOS velocities from different tracks leads to sensible results. As shown in Figure 4, the results are further improved when using four overlapping InSAR frames.

RMSE increases slightly with increasing V_n , this is likely due to the parallel increase of input errors in the tests. In general, the ratio of the three velocity components has minor impact on the RMSE, but fast deformation in the other directions can cause systematic shifting of the inverted signal. A shift of N-S velocities towards positive values (motion to the north) is observable, independent of vertical velocities and LOS noise, hence we interpret that the fast westward movement of Anatolia, which is also simulated in the synthetic velocities, induces a false northward signal. This shift minimally affects velocity gradients across faults, but it needs to be considered when interpreting absolute velocities. Similarly, the constant subsidence modelled in the tests appears to induce a false negative signal in the inversion for V_n .

When solving for vertical deformation (V_u), its absolute value decreases with increasing V_e , whereas V_n does not appear to influence it. Owing to the higher sensitivity to vertical deformation, the shift induced to V_u is ≤ 0.25 mm/yr across all tests, while it can be up to 8 mm/yr for V_n . Elevated noise generally results in systematic errors in all tests.

5.2 North-South Deformation

The inverted N-S deformation field for the study area in its current state is not sufficient to quantify deformation rates for individual faults or determine the most active fault zones. The central part, covered by four overlapping frames, shows the most realistic and consistent deformation rates. Based on these results and insights from synthetic tests, the following criteria are outlined for successful inversion of the N-S component: (1) maximum noise $\sim 5\%$ in the LOS velocities; (2) a study site covered by at least three, better four overlapping Sentinel-1 frames; (3) relatively low V_e and V_u , which can induce systematic errors, and (4) a discrete, fast N-S deformation signal (e.g., a N-S trending strike-slip fault), which is easier to quantify than deformation distributed over multiple fault zones. Additionally, we encourage the use of synthetic data tests (not only when solving for V_n), which are easy to perform and can provide valuable insights, including potential systematic errors which otherwise go unnoticed. Synthetic tests can be adapted to specific study conditions.

5.3 Vertical Deformation

5.3.1 Accuracy of Velocity

The propagated standard deviation of our inverted vertical velocities (Fig. 6b) is in the range of 0-1 mm/yr, though the real deviation could be larger. We compare our vertical velocity rates with those determined by other studies. Poyraz et al. (2019) and Poyraz and Hastaoğlu (2020) determined deformation rates in the eastern Gediz graben from GNSS and persistent scatterer InSAR (PSInSAR). Vertical deformation from multiple sensors is also available for several coastal locations (Erkoç et al., 2022); however, comparison with these data is less accurate owing to decorrelation in the coastal areas (see Supplement 2). For comparison with other studies, we average InSAR velocities in a box of ~ 1 km around the sites of other studies, error bars display three standard deviations of the averaged velocities. The InSAR velocities are lower (more negative) than the GNSS and PSInSAR velocities at most locations (Fig. 9). If GNSS/PSInSAR velocities are more accurate than InSAR, and the observed differences are representative for the entire study region, uplift rates could be systematically underestimated in our study by several mm/yr. For the broad deformation field, this would not make a notable

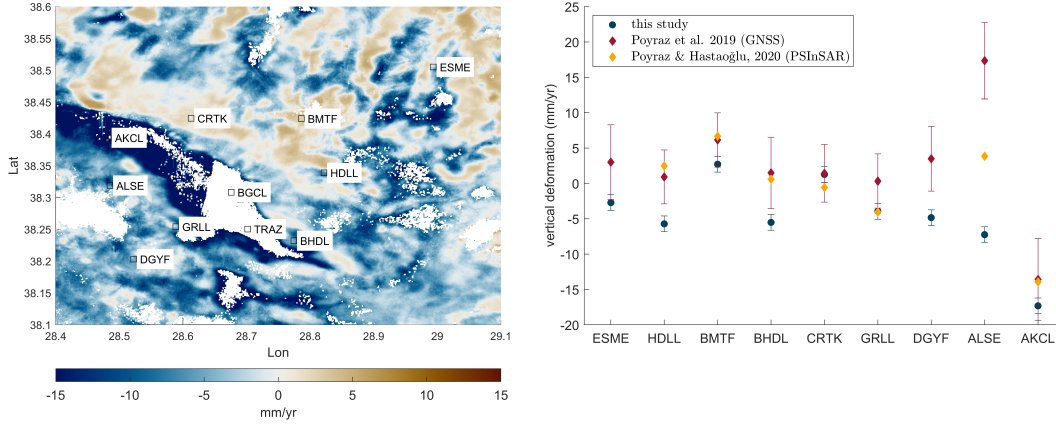


Figure 9. Comparison of vertical deformation rates from InSAR (this study) to GNSS (Poyraz et al., 2019) and persistent scatterer InSAR (Poyraz & Hastaoğlu, 2020) for nine locations in the eastern Gediz Graben.

difference, however slip rates at individual faults would be faster than the rates we observe.

Short term deformation rates (GNSS, InSAR, PSInSAR) are ~ 5 times faster than long-term rates from cross-section profiles or river profile analysis (Kent et al., 2017, 2020) and ^{36}Cl -dating (Mozafari et al., 2022), depending on the conversion from uplift to throw/slip rates. Long-term slip rates average deformation over multiple seismic cycles, whereas InSAR velocities represent short-term movements within the interseismic period. Accordingly, uplift rates and respective throw rates of faults from InSAR are not necessarily representative of the long-term throw rates and should not be used for modelling interseismic deformation or estimating earthquake recurrence times.

5.3.2 Tectonic vs. Non-Tectonic Signals

Where the uplift signal correlates spatially with fault traces, we are confident that the observed deformation is due to tectonic processes. The topographic contrast between footwall and hangingwall at many of the fast-deforming faults, e.g., the Halitpaşa fault in the Gediz Graben, is negligible. So the clear deformation signal along the fault scarp cannot be attributed to topographic or atmospheric effects. Our data generally agree with the non-tectonic deformation signals found by other studies. However, as these almost exclusively focus on the subsidence in grabens, we are unable to confirm deformation rates due to large uncertainties and decorrelation of the InSAR velocities in the grabens.

5.3.3 Vertical Deformation Rates

Footwall uplift along active faults in the study region (Figs. 6 & 8, table 2) varies significantly. Most of the known active faults show a clear tectonic deformation signal along the mapped fault traces. However, several known active faults show no detectable deformation signal. Fault slip rates vary over a range of timescales, influenced by fault linkage, interaction with other faults, and earthquake clustering (Cowie & Roberts, 2001; Friedrich et al., 2003; Mildon et al., 2022). Therefore we suggest that these faults with no detectable deformation signal should not be considered inactive on the basis of our study, and instead we hypothesise that these faults could be undergoing a period of lower deformation/slip rate.

Detailed investigation of active faulting in the Gediz region (Fig. 8) further highlights the following aspects relevant to the regional seismic hazard: (1) The antithetic

faults, commonly considered less important, show faster deformation over the studied time period than the main graben bounding fault and therefore should be considered as equal seismic hazard potential. (2) The old, low-angle detachment fault, contrary to established belief, appears to be active as there is a change in uplift rate coincident with the fault trace. (3) The GGBF has spatial correlation between current deformation rate and the 1969 M_W 6.9 earthquake on the Alasehir segment, which is not observable in long-term throw rates of the fault segments (Kent et al., 2017). We interpret that the reduced deformation rate at the ruptured segment relates to stress released due to the earthquake. If correct, this would imply that the other segments are still stressed, and potentially capable of producing a damaging earthquake of similar magnitude. (4) Fault zones constantly evolve and the active fault splays can be far from the mapped active fault trace, most clearly seen at the Manisa fault. While using geological mapping and geomorphological analyses may be challenging to identify these shifts in the location of deformation and active faulting, the InSAR velocity is able to detect the active deformation on unknown faults or fault branches.

6 Conclusions

In the first part of the study, we outline the potential of currently available Sentinel-1 InSAR datasets to extract N-S surface deformation rates. We present an approach using a combination of synthetic tests and real data and an over-determined inversion process to constrain the north component of deformation as accurately as possible. At the current state the technique is suitable to detect trends/patterns of deformation and give an idea of the regional deformation, though improvements are needed to quantify deformation rates on individual faults.

Our synthetic tests show that the key factor for successful derivation of N-S motions is the signal/noise ratio. With potential future improvements, this technique can become applicable, at least in selected study sites that meet the criteria we outline. We encourage the use of tests with synthetic data, not only for extraction of the N-S component, but also for E-W and vertical. These are easy to perform and can provide insight into biases due to other velocity components.

The overarching objective of this study is to investigate the deformation field of the Western Anatolian Extensional Province with respect to active normal faults. Regional fault activity varies both spatially and temporally. We observe surface deformation at the majority of faults in the WAEP, with apparent footwall uplift up to ~ 5 mm/yr. We demonstrate that vertical deformation can be used to determine faults/branches that were previously not inferred to be active, including low-angle normal faults along the Gediz Graben, or the newly detected fault splay of the Manisa fault. Finally, we show a possible correlation between active deformation at the Gediz Graben boundary faults and the 1969 rupture with potential implications for seismic hazard of the other segments.

7 Open Research

All used interferograms are available via the COMET LiCS portal at <https://comet.nerc.ac.uk/comet-lics-portal/> (Lazecý et al., 2020) and were processed with the open-source software LiCSBAS, available via <https://github.com/yumorishita/LiCSBAS> (Morishita et al., 2020).

Acknowledgments

We thank Jonathan Weiss for insightful discussions on N-S deformation. M.D. is supported by a University of Plymouth, School of Geography, Earth and Environmental Sciences PhD studentship. E.H. is supported by the BGS International National Capability programme ‘Geoscience to tackle Global Environmental Challenges’, NERC reference

NE/X006255/1 and the Royal Society project RGS.R2.212091. The paper is published by permission of the Director of the British Geological Survey.

References

- Aktug, B., Nocquet, J. M., Cingöz, A., Parsons, B., Erkan, Y., England, P., ... Tekgül, A. (2009, October). Deformation of western Turkey from a combination of permanent and campaign GPS data: Limits to block-like behavior. *Journal of Geophysical Research*, 114(B10), B10404. doi: 10.1029/2008JB006000
- Alçıçek, M. C., Ten Veen, J., & Özkul, M. (2006). Neotectonic development of the Cameli Basin, southwestern Anatolia, Turkey. *ROBERTSON, A. H. F. & MOUNTRAKIS, D. (eds) 2006. Tectonic Development of the Eastern Mediterranean Region. Geological Society, London, Special Publications, 260, 591–611.*
- Arpat, E., & Bingöl, E. (1969, February). Ege Bölgesi graben sisteminin gelişimi üzerine düşünceler [in Turkish]. *Bulletin of the Mineral Research and Exploration*, 73(73), 1–9.
- Aslan, G., Aydin, H., & Çakir, Z. (2022, January). Wide-area ground deformation monitoring in geothermal fields in western Turkey. *Turkish Journal of Earth Sciences*, 31(3), 247–259. doi: 10.55730/1300-0985.1771
- Bozkurt, E., & Sözbilir, H. (2004, January). Tectonic evolution of the Gediz Graben: Field evidence for an episodic, two-stage extension in western Turkey. *Geological Magazine*, 141(1), 63–79. doi: 10.1017/S0016756803008379
- Çiftçi, N. B., & Bozkurt, E. (2009, July). Pattern of normal faulting in the Gediz Graben, SW Turkey. *Tectonophysics*, 473(1-2), 234–260. doi: 10.1016/j.tecto.2008.05.036
- Cowie, P. A., & Roberts, G. P. (2001, December). Constraining slip rates and spacings for active normal faults. *Journal of Structural Geology*, 23(12), 1901–1915. doi: 10.1016/S0191-8141(01)00036-0
- Doğan, A., Kaygusuz, Ç., Tiryakioğlu, İ., Yigit, C. O., Sözbilir, H., Özkaymak, Ç., & Turgut, B. (2022, September). Geodetic evidence for aseismic fault movement on the eastern segment of the Gediz Graben system (western Anatolia extensional province, Turkey) and its significance for settlements. *Acta Geodaetica et Geophysica*, 57(3), 461–476. doi: 10.1007/s40328-022-00389-1
- Emre, Ö., Duman, T. Y., Özalp, S., Şaroğlu, F., Olgun, Ş., Elmacı, H., & Çan, T. (2018, August). Active fault database of Turkey. *Bulletin of Earthquake Engineering*, 16(8), 3229–3275. doi: 10.1007/s10518-016-0041-2
- England, P., Houseman, G., & Nocquet, J.-M. (2016). Constraints from GPS measurements on the dynamics of deformation in Anatolia and the Aegean. *Journal of Geophysical Research: Solid Earth*, 121(12), 8888–8916. doi: 10.1002/2016JB013382
- Erkoç, M. H., Doğan, U., Yıldız, H., & Sezen, E. (2022, October). Estimation of vertical land motion along the south and west coast of Turkey from multi-sensor observations. *Advances in Space Research*, 70(7), 1761–1772. doi: 10.1016/j.asr.2022.06.022
- Eyidoğan, H., & Jackson, J. (1985, June). A seismological study of normal faulting in the Demirci, Alaşehir and Gediz earthquakes of 1969–70 in western Turkey: Implications for the nature and geometry of deformation in the continental crust. *Geophysical Journal International*, 81(3), 569–607. doi: 10.1111/j.1365-246X.1985.tb06423.x
- Fialko, Y., Simons, M., & Agnew, D. (2001). The complete (3-D) surface displacement field in the epicentral area of the 1999 MW7.1 Hector Mine Earthquake, California, from space geodetic observations. *Geophysical Research Letters*, 28(16), 3063–3066. doi: 10.1029/2001GL013174

- Friedrich, A. M., Wernicke, B. P., Niemi, N. A., Bennett, R. A., & Davis, J. L. (2003). Comparison of geodetic and geologic data from the Wasatch region, Utah, and implications for the spectral character of Earth deformation at periods of 10 to 10 million years. *Journal of Geophysical Research: Solid Earth*, 108(B4). doi: 10.1029/2001JB000682
- Ganas, A., Oikonomou, I. A., & Tsimi, C. (2013). NOAfaults: A digital database for active faults in Greece. *Bulletin of the Geological Society of Greece*, 47(2), 518. doi: 10.12681/bgsg.11079
- Ganas, A., Sakellariou, D., Tsironi, V., Tsampouraki-Kraounaki, K., Papaioannou, C., Konstantakopoulou, E., . . . Loukaidi, V. (2023, May). *The HELPOS Fault Database: A new contribution to seismic hazard assessment in Greece*. Zenodo. doi: 10.5281/zenodo.7938340
- Gessner, K., Ring, U., Johnson, C., Hetzel, R., Passchier, C. W., & GÜNGÖR, T. (2001). An active bivergent rolling-hinge detachment system: Central Menderes metamorphic core complex in western Turkey. *Geology*, 29(7), 611. doi: 10.1130/0091-7613(2001)029{\$}\$0611:AABRHD{\$}\$2.0.CO;2
- Hastaoglu, K. O., Poyraz, F., Erdogan, H., Tiryakioglu, İ., Ozkaymak, C., Duman, H., . . . Gul, Y. (2023, May). Determination of periodic deformation from InSAR results using the FFT time series analysis method in Gediz Graben. *Natural Hazards*, 117(1), 491–517. doi: 10.1007/s11069-023-05870-w
- Hooper, A., Bekaert, D., Spaans, K., & Arıkan, M. (2012, January). Recent advances in SAR interferometry time series analysis for measuring crustal deformation. *Tectonophysics*, 514–517, 1–13. doi: 10.1016/j.tecto.2011.10.013
- Hu, J., Li, Z. W., Ding, X. L., Zhu, J. J., Zhang, L., & Sun, Q. (2014, June). Resolving three-dimensional surface displacements from InSAR measurements: A review. *Earth-Science Reviews*, 133, 1–17. doi: 10.1016/j.earscirev.2014.02.005
- Hussain, E., Wright, T. J., Walters, R. J., Bekaert, D., Hooper, A., & Houseman, G. A. (2016). Geodetic observations of postseismic creep in the decade after the 1999 Izmit earthquake, Turkey: Implications for a shallow slip deficit. *Journal of Geophysical Research: Solid Earth*, 121(4), 2980–3001. doi: 10.1002/2015JB012737
- Hussain, E., Wright, T. J., Walters, R. J., Bekaert, D. P. S., Lloyd, R., & Hooper, A. (2018, April). Constant strain accumulation rate between major earthquakes on the North Anatolian Fault. *Nature Communications*, 9(1), 1392. doi: 10.1038/s41467-018-03739-2
- Imamoglu, M., Balik Sanli, F., Cakir, Z., & Kahraman, F. (2022, April). Rapid ground subsidence in the Küçük Menderes Graben (W. Turkey) captured by Sentinel-1 SAR data. *Environmental Earth Sciences*, 81(7), 221. doi: 10.1007/s12665-022-10339-3
- Jackson, J. (1994). Active Tectonics of the Aegean Region. *Annual Review of Earth and Planetary Sciences*, 22(239), 33.
- Kent, E., Boulton, S. J., Stewart, I. S., Whittaker, A. C., & Alçiçek, M. C. (2016, July). Geomorphic and geological constraints on the active normal faulting of the Gediz (Alaşehir) Graben, Western Turkey. *Journal of the Geological Society*, 173(4), 666–678. doi: 10.1144/jgs2015-121
- Kent, E., Boulton, S. J., Whittaker, A. C., Stewart, I. S., & Cihat Alçiçek, M. (2017). Normal fault growth and linkage in the Gediz (Alaşehir) Graben, Western Turkey, revealed by transient river long-profiles and slope-break knickpoints. *Earth Surface Processes and Landforms*, 42(5), 836–852. doi: 10.1002/esp.4049
- Kent, E., Whittaker, A., Boulton, S., & Alçiçek, M. (2020). Quantifying the competing influences of lithology and throw rate on bedrock river incision. *GSA Bulletin*, 133(7-8), 1649–1664. doi: 10.1130/B35783.1
- Koca, Y., Sözbilir, H., & Uzel, B. (2011, December). Sarıgöl Fay Zonu Boyunca

- Meydana Gelen Deformasyonların Nedenleri Üzerine Bir Araştırma. *Jeoloji Mühendisliği Dergisi*, 35(2), 151–174.
- Koçyiğit, A. (2005, August). The Denizli graben-horst system and the eastern limit of western Anatolian continental extension: Basin fill, structure, deformational mode, throw amount and episodic evolutionary history, SW Turkey. *Geodinamica Acta*, 18(3-4), 167–208. doi: 10.3166/ga.18.167-208
- Kurt, A. İ., Özbakir, A. D., ÇiNGöz, A., ErgiNtav, S., Doğan, U., & Özarpacı, S. (2023, January). Contemporary Velocity Field for Turkey Inferred from Combination of a Dense Network of Long Term GNSS Observations. *Turkish Journal of Earth Sciences*, 32(3), 275–293. doi: 10.55730/1300-0985.1844
- Lazecký, M., Spaans, K., González, P. J., Maghsoudi, Y., Morishita, Y., Albino, F., ... Wright, T. J. (2020, January). LiCSAR: An Automatic InSAR Tool for Measuring and Monitoring Tectonic and Volcanic Activity. *Remote Sensing*, 12(15), 2430. doi: 10.3390/rs12152430
- Manzocchi, T., Walsh, J. J., & Nicol, A. (2006, September). Displacement accumulation from earthquakes on isolated normal faults. *Journal of Structural Geology*, 28(9), 1685–1693. doi: 10.1016/j.jsg.2006.06.006
- McClusky, S., Balassanian, S., Barka, A., Demir, C., Ergintav, S., Georgiev, I., ... Veis, G. (2000). Global Positioning System constraints on plate kinematics and dynamics in the eastern Mediterranean and Caucasus. *Journal of Geophysical Research: Solid Earth*, 105(B3), 5695–5719. doi: 10.1029/1999JB900351
- McKenzie, D. (1972, December). Active Tectonics of the Mediterranean Region. *Geophysical Journal International*, 30(2), 109–185. doi: 10.1111/j.1365-246X.1972.tb02351.x
- McKenzie, D. (1978, October). Active tectonics of the Alpine—Himalayan belt: The Aegean Sea and surrounding regions. *Geophysical Journal International*, 55(1), 217–254. doi: 10.1111/j.1365-246X.1978.tb04759.x
- Mildon, Z. K., Roberts, G. P., Faure Walker, J. P., Beck, J., Papanikolaou, I., Michetti, A. M., ... Vittori, E. (2022, November). Surface faulting earthquake clustering controlled by fault and shear-zone interactions. *Nature Communications*, 13(1), 7126. doi: 10.1038/s41467-022-34821-5
- Morishita, Y., Lazecky, M., Wright, T., Weiss, J., Elliott, J., & Hooper, A. (2020, January). LiCSBAS: An Open-Source InSAR Time Series Analysis Package Integrated with the LiCSAR Automated Sentinel-1 InSAR Processor. *Remote Sensing*, 12(3), 424. doi: 10.3390/rs12030424
- Mozafari, N., Özkaymak, Ç., Sümer, Ö., Tikhomirov, D., Uzel, B., Yeşilyurt, S., ... Akçar, N. (2022, December). Seismic history of western Anatolia during the last 16 kyr determined by cosmogenic ³⁶Cl dating. *Swiss Journal of Geosciences*, 115(1), 5. doi: 10.1186/s00015-022-00408-x
- Nocquet, J.-M. (2012, December). Present-day kinematics of the Mediterranean: A comprehensive overview of GPS results. *Tectonophysics*, 579, 220–242. doi: 10.1016/j.tecto.2012.03.037
- Özdemir, S., & Karshoğlu, M. O. (2019, August). Soft clustering of GPS velocities from a homogeneous permanent network in Turkey. *Journal of Geodesy*, 93(8), 1171–1195. doi: 10.1007/s00190-019-01235-z
- Özkaymak, Ç., Sozbilir, H., Geçievi, M. O., & Tiryakioğlu, İ. (2019). Late Holocene coseismic rupture and aseismic creep on the Bolvadin Fault, Afyon Akşehir Graben, Western Anatolia. *TURKISH JOURNAL OF EARTH SCIENCES*. doi: 10.3906/yer-1906-13
- Poyraz, F., Hastaoğlu, K., Koçbulut, F., Tiryakioğlu, I., Tatar, O., Demirel, M., ... Sıgırcı, R. (2019, January). Determination of the block movements in the eastern section of the Gediz Graben (Turkey) from GNSS measurements. *Journal of Geodynamics*, 123, 38–48. doi: 10.1016/j.jog.2018.11.001
- Poyraz, F., & Hastaoğlu, K. Ö. (2020, September). Monitoring of tectonic movements of the Gediz Graben by the PSInSAR method and validation

- with GNSS results. *Arabian Journal of Geosciences*, 13(17), 844. doi: 10.1007/s12517-020-05834-5
- Purvis, M., & Robertson, A. (2004, October). A pulsed extension model for the Neogene–Recent E–W-trending Alaşehir Graben and the NE–SW-trending Selendi and Gördes Basins, western Turkey. *Tectonophysics*, 391(1), 171–201. doi: 10.1016/j.tecto.2004.07.011
- Roberts, G. P. (2007, January). Fault orientation variations along the strike of active normal fault systems in Italy and Greece: Implications for predicting the orientations of subseismic-resolution faults in hydrocarbon reservoirs. *AAPG Bulletin*, 91(1), 1–20. doi: 10.1306/08300605146
- Samsonov, S., Tiampo, K., & Rundle, J. (2008, May). Application of DInSAR-GPS optimization for derivation of three-dimensional surface motion of the southern California region along the San Andreas fault. *Computers & Geosciences*, 34(5), 503–514. doi: 10.1016/j.cageo.2007.05.013
- Schlagenhauf, A., Manighetti, I., Malavieille, J., & Dominguez, S. (2008, September). Incremental growth of normal faults: Insights from a laser-equipped analog experiment. *Earth and Planetary Science Letters*, 273(3), 299–311. doi: 10.1016/j.epsl.2008.06.042
- Seyitoğlu, G., & Işık, V. (2009). Meaning of the Küçük Menderes graben in the tectonic framework of the central Menderes metamorphic core complex (western Turkey). *Geologica Acta*, 7(3), 9.
- Seyitoğlu, G., Tekeli, O., Çemen, İ., Şen, Ş., & Işık, V. (2002, January). The role of the flexural rotation/rolling hinge model in the tectonic evolution of the Alaşehir graben, western Turkey. *Geological Magazine*, 139(1), 15–26. doi: 10.1017/S0016756801005969
- Taymaz, T., Yilmaz, Y., & Dilek, Y. (2007, January). The geodynamics of the Aegean and Anatolia: Introduction. *Geological Society, London, Special Publications*, 291(1), 1–16. doi: 10.1144/SP291.1
- Ten Veen, J., Boulton, S., & Alçiçek, M. (2009, July). From palaeotectonics to neotectonics in the Neotethys realm: The importance of kinematic decoupling and inherited structural grain in SW Anatolia (Turkey). *Tectonophysics*, 473(1-2), 261–281. doi: 10.1016/j.tecto.2008.09.030
- Uzel, B., Sözbilir, H., Özkaymak, Ç., Kaymakcı, N., & Langereis, C. G. (2012). Structural evidence for strike-slip deformation in the İzmir–Balıkesir transfer zone and consequences for late Cenozoic evolution of western Anatolia (Turkey). *Journal of Geodynamics*, 65, 94–116. doi: 10.1016/j.jog.2012.06.009
- Vollrath, A., Zucca, F., Bekaert, D., Bonforte, A., Guglielmino, F., Hooper, A. J., & Stramondo, S. (2017, January). Decomposing DInSAR Time-Series into 3-D in Combination with GPS in the Case of Low Strain Rates: An Application to the Hyblean Plateau, Sicily, Italy. *Remote Sensing*, 9(1), 33. doi: 10.3390/rs9010033
- Weiss, J. R., Walters, R. J., Morishita, Y., Wright, T. J., Lazecky, M., Wang, H., . . . Parsons, B. (2020, September). High-Resolution Surface Velocities and Strain for Anatolia From Sentinel-1 InSAR and GNSS Data. *Geophysical Research Letters*, 47(17). doi: 10.1029/2020GL087376
- Wright, T. J., Parsons, B. E., & Lu, Z. (2004). Toward mapping surface deformation in three dimensions using InSAR. *Geophysical Research Letters*, 31(1). doi: 10.1029/2003GL018827
- Yang, J., Xu, C., Wang, S., & Wang, X. (2020, April). Sentinel-1 observation of 2019 Mw 5.7 Acipayam earthquake: A blind normal-faulting event in the Acipayam basin, southwestern Turkey. *Journal of Geodynamics*, 135, 101707. doi: 10.1016/j.jog.2020.101707
- Yu, C., Li, Z., Penna, N. T., & Crippa, P. (2018). Generic Atmospheric Correction Model for Interferometric Synthetic Aperture Radar Observations. *Jour-*

695 *nal of Geophysical Research: Solid Earth*, 123(10), 9202–9222. doi: 10.1029/
696 2017JB015305

Figure 01.

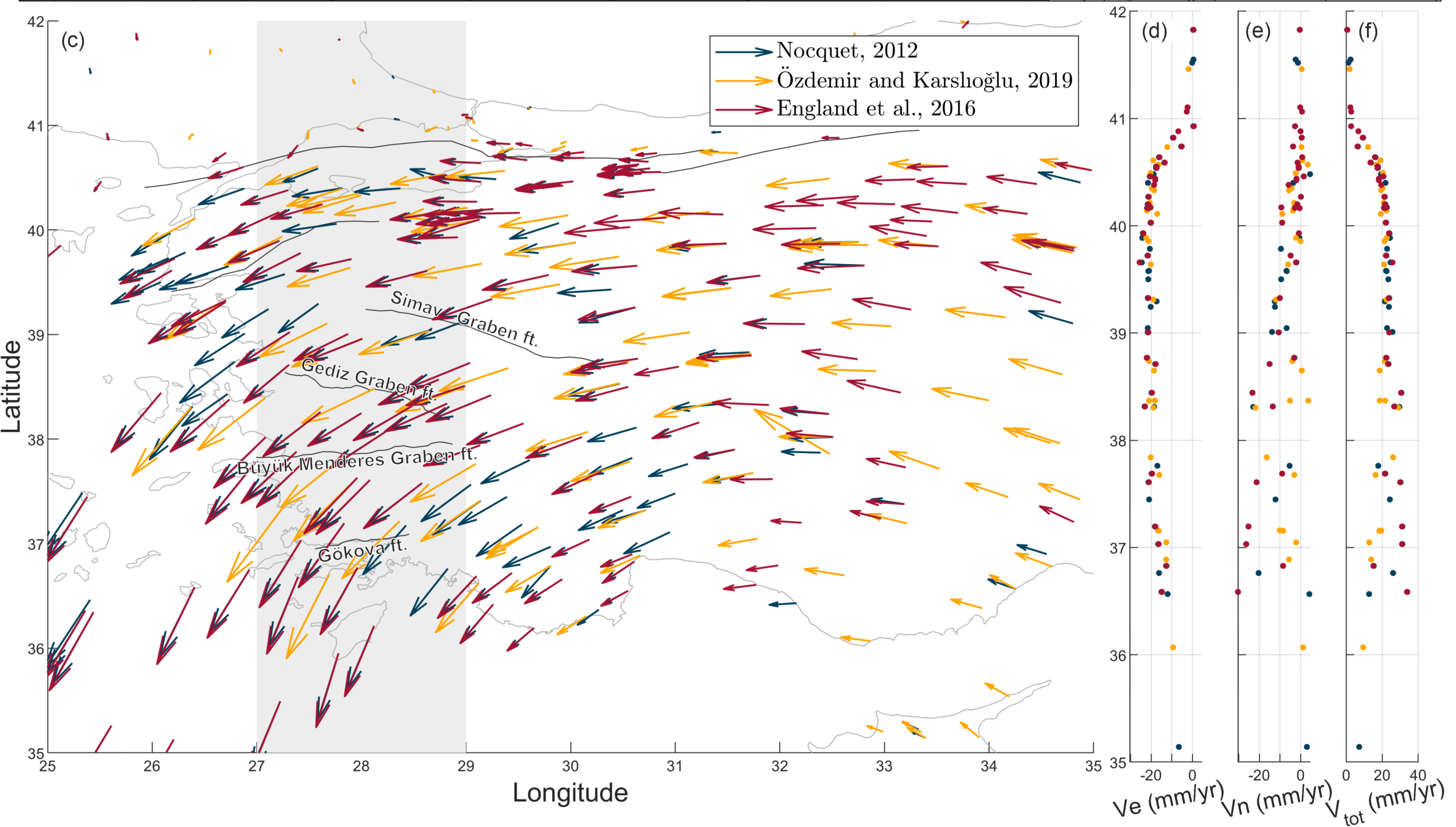
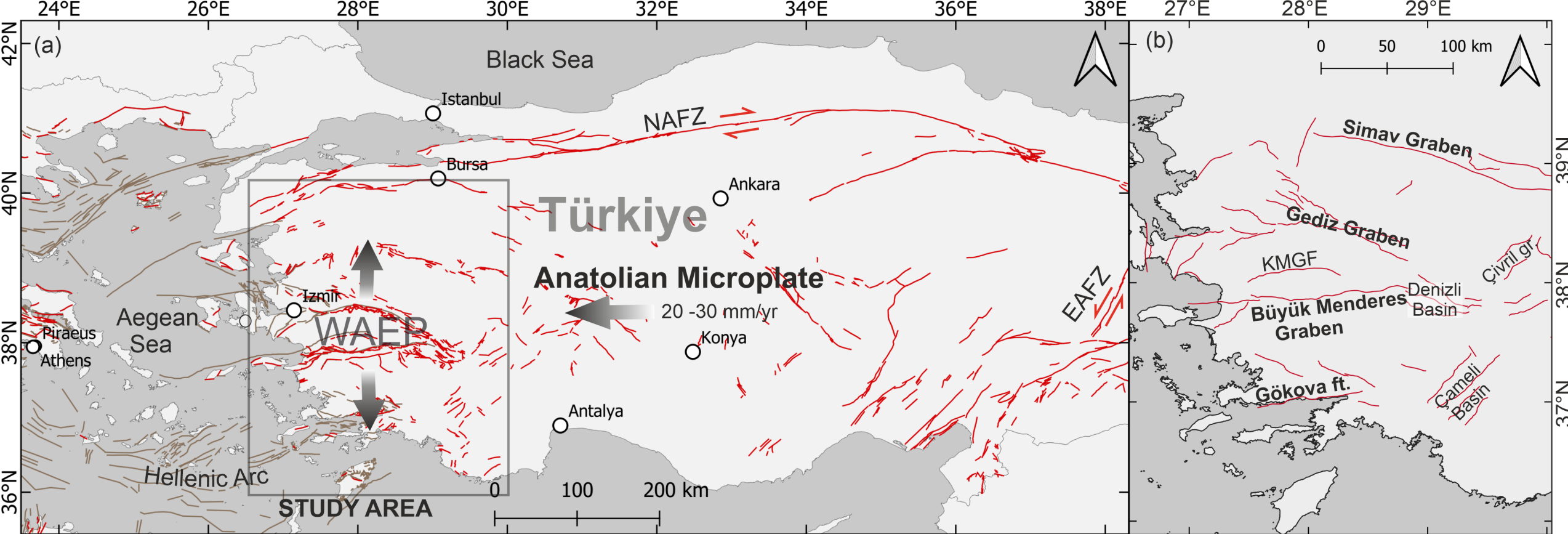


Figure 02.

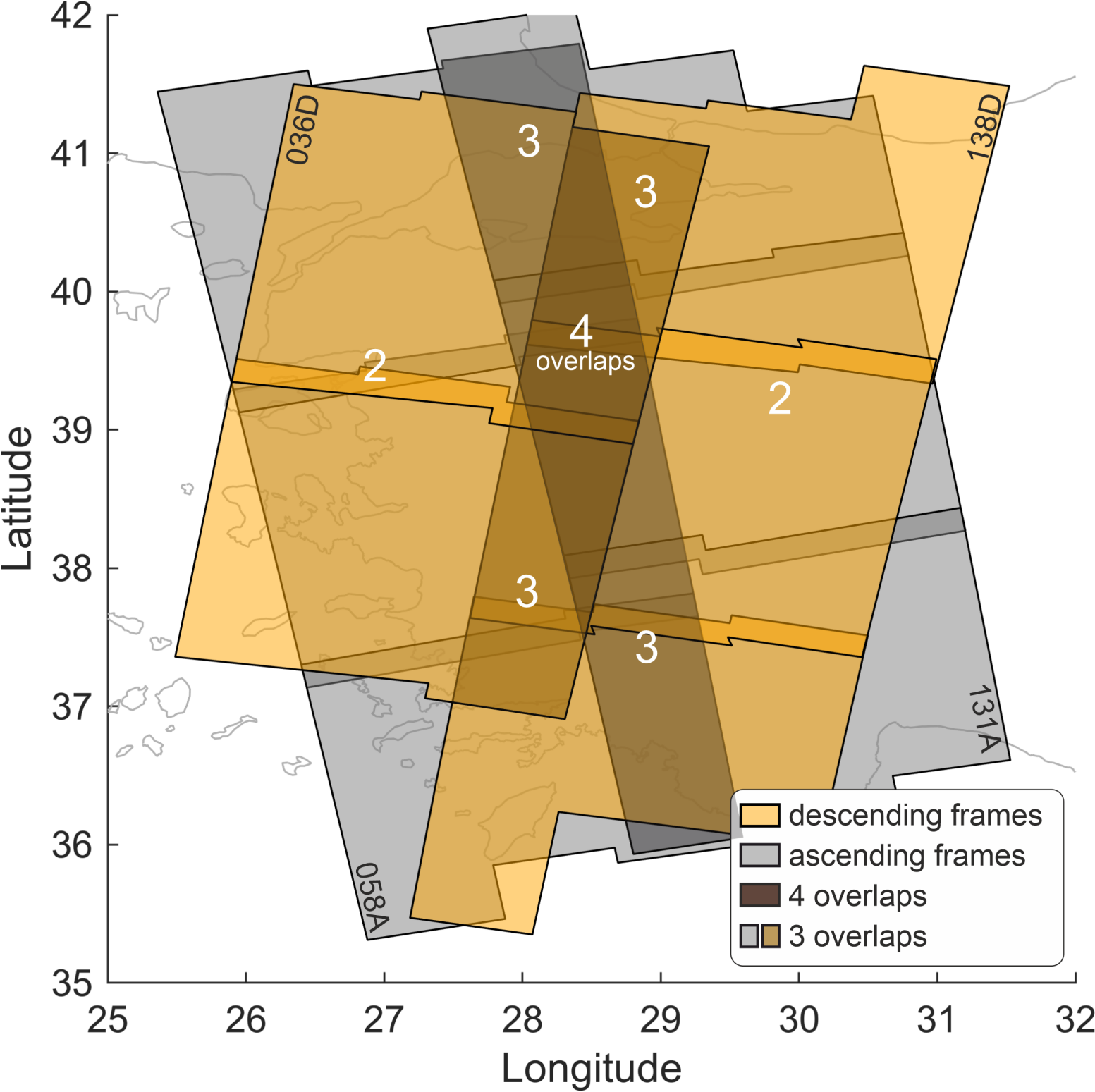
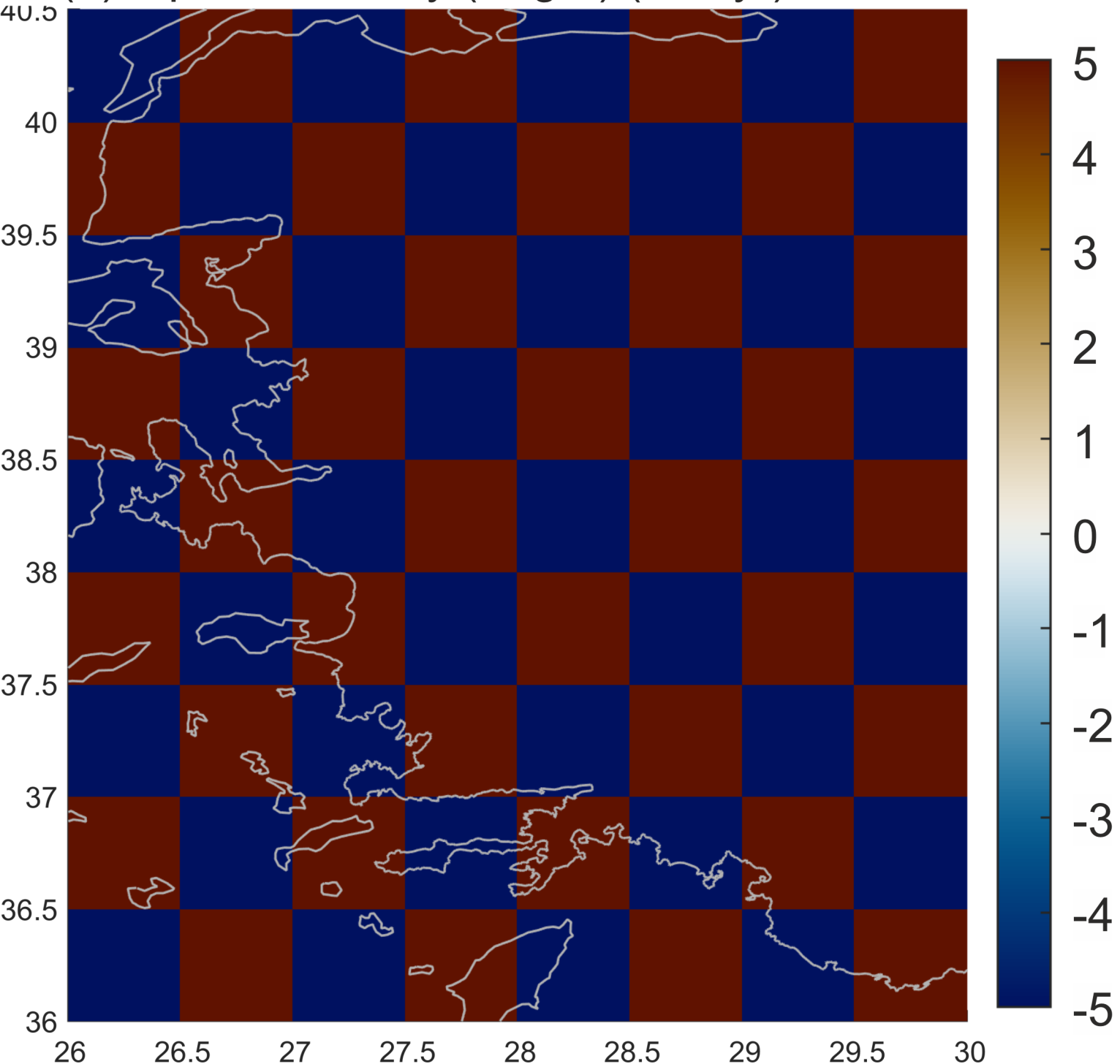
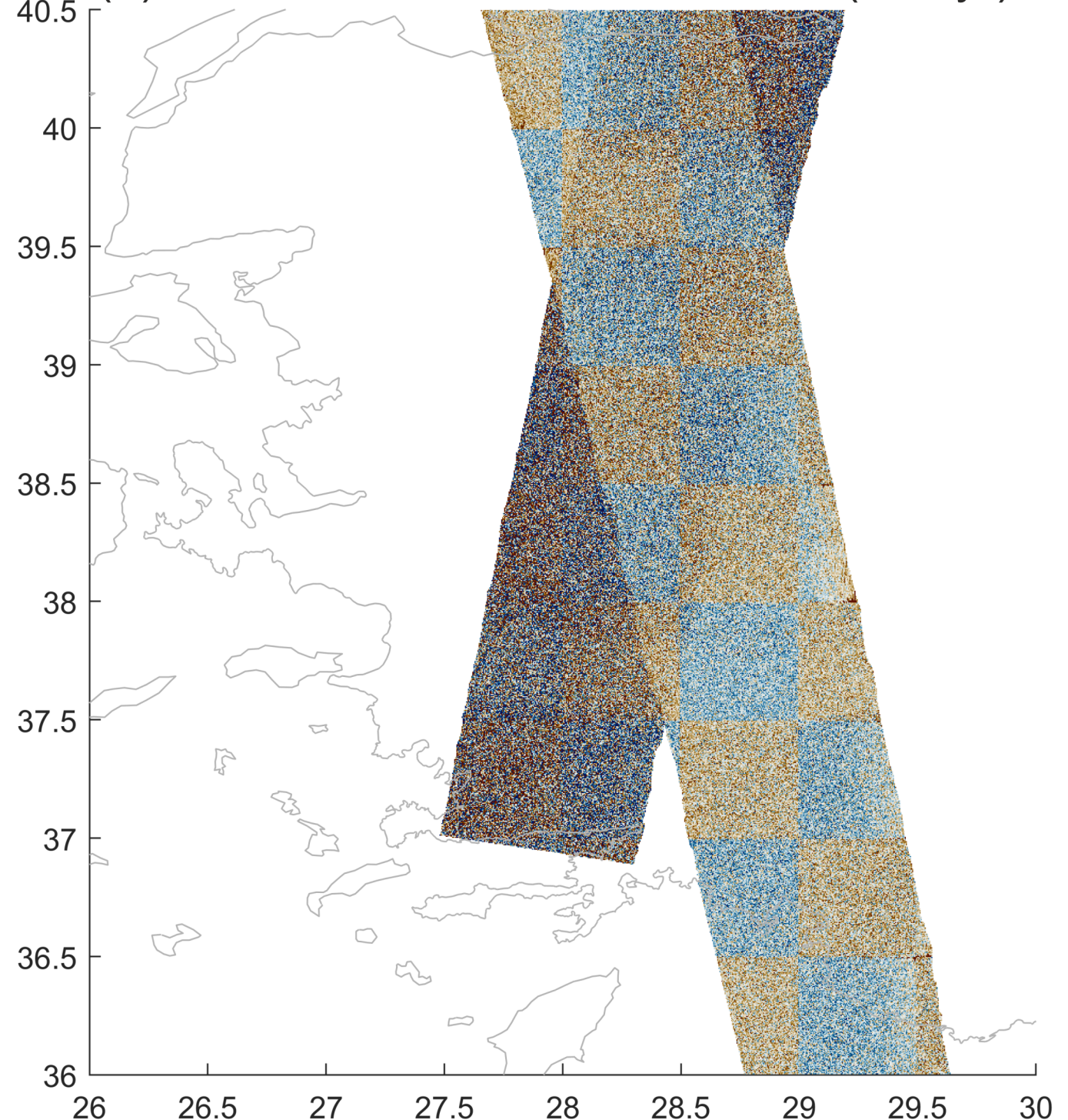


Figure 03.

(a) Input N velocity (target) (mm/yr)



(b) inversion result 5% LOS noise (mm/yr)



(c) inversion result 20% LOS noise (mm/yr)

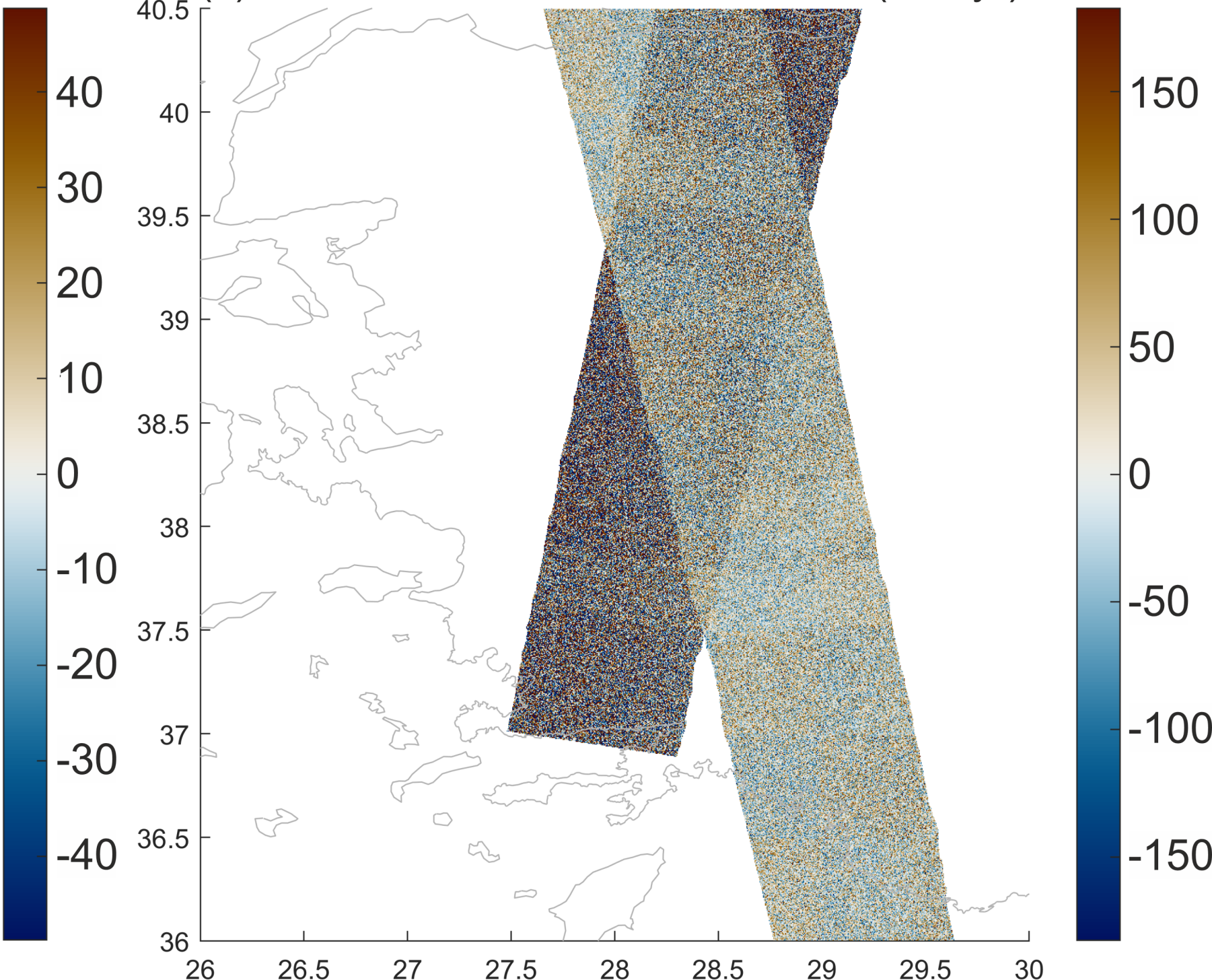


Figure 04.

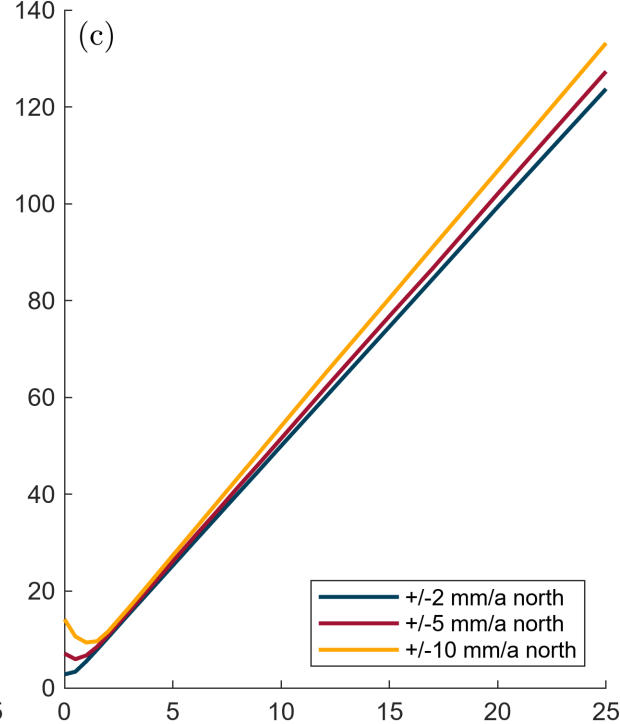
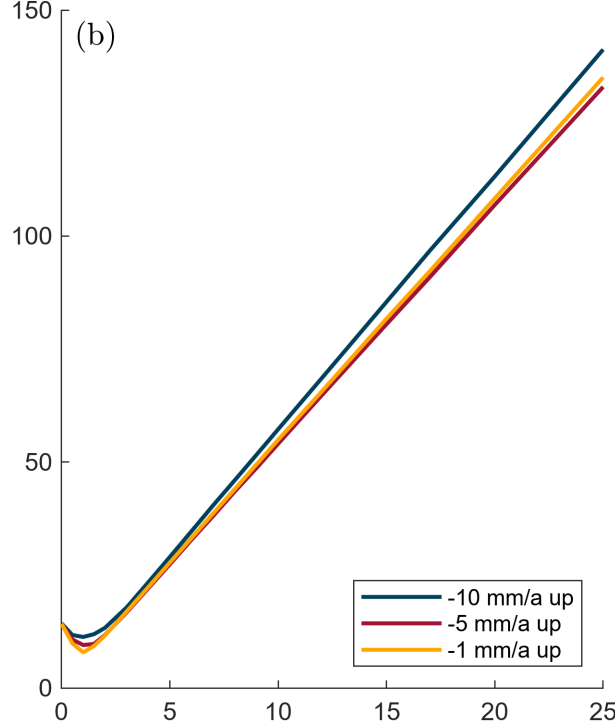
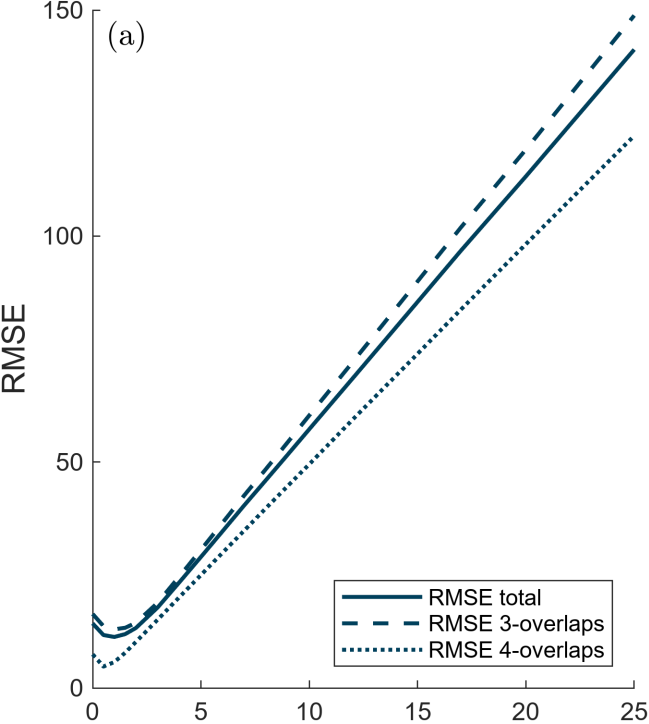


Figure 05.

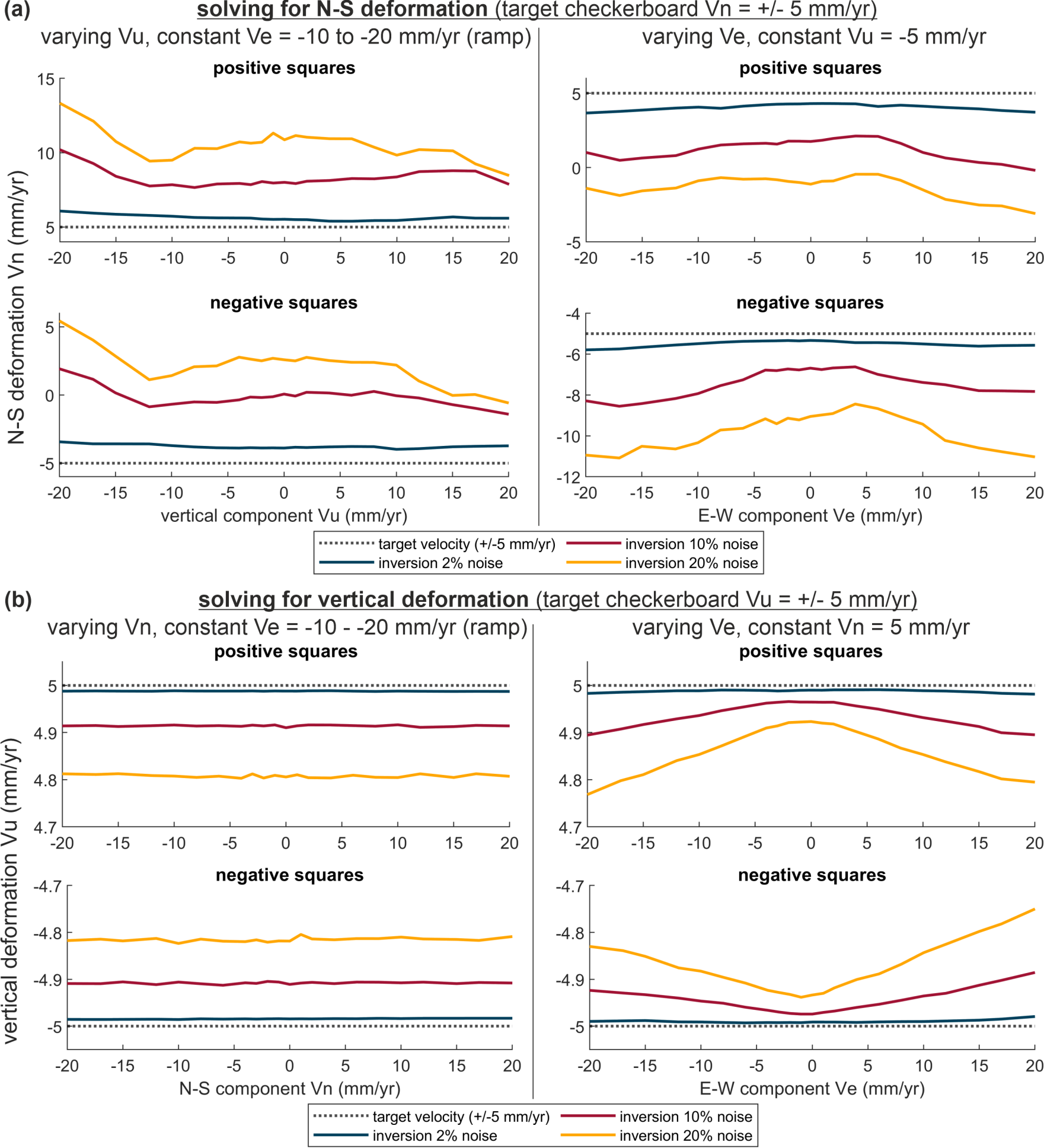


Figure 06.

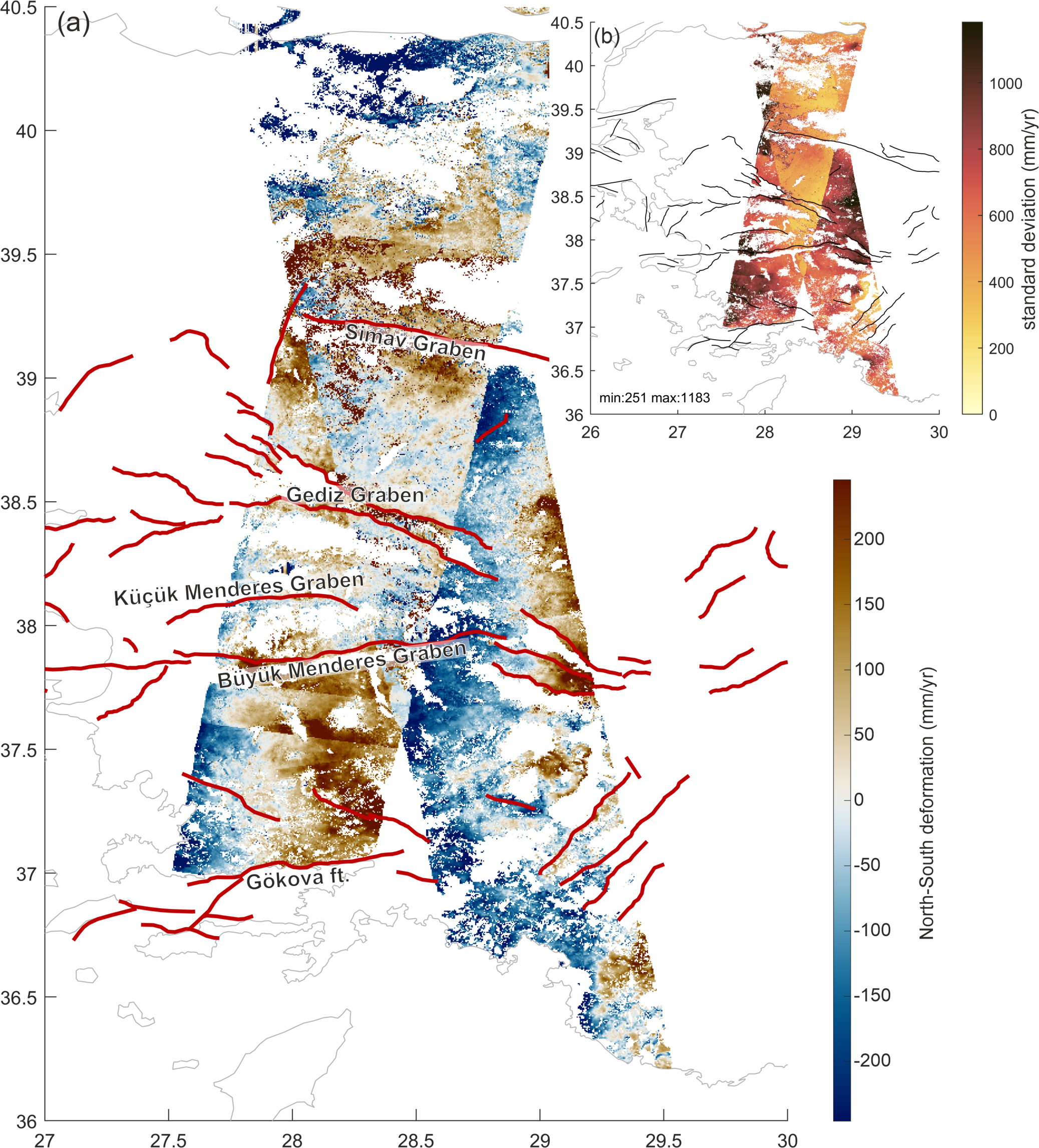


Figure 07.

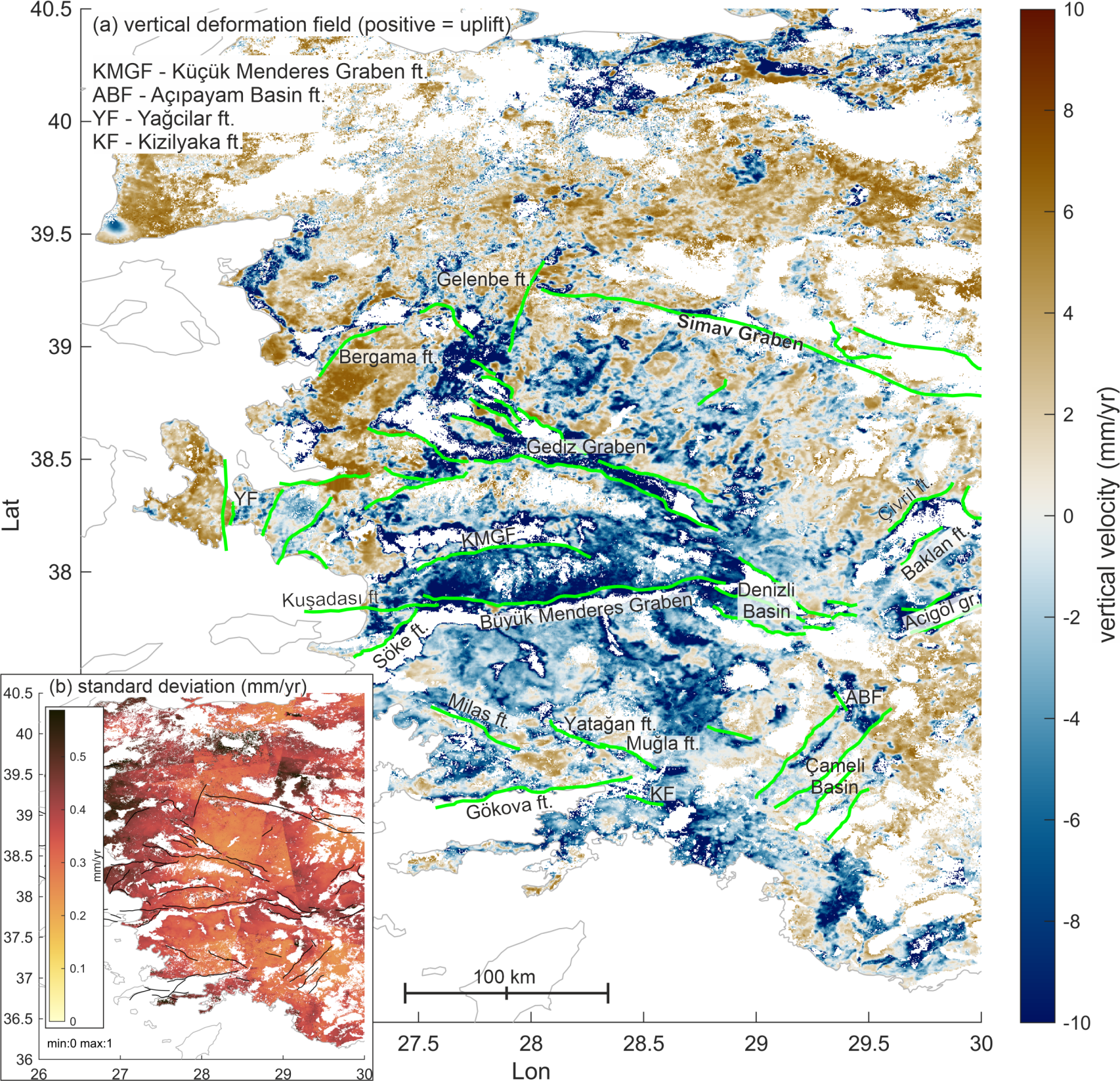


Figure 08.

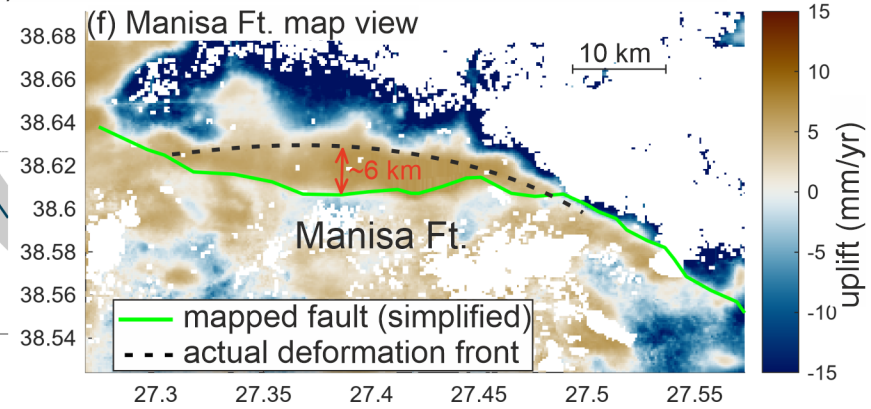
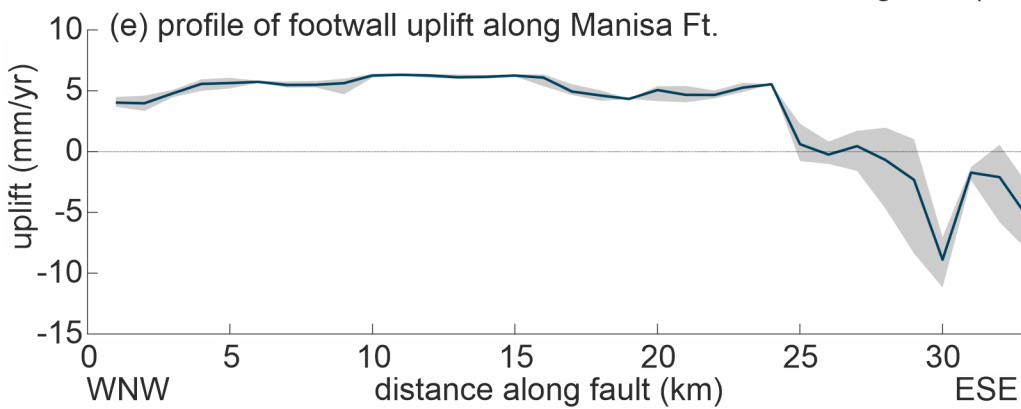
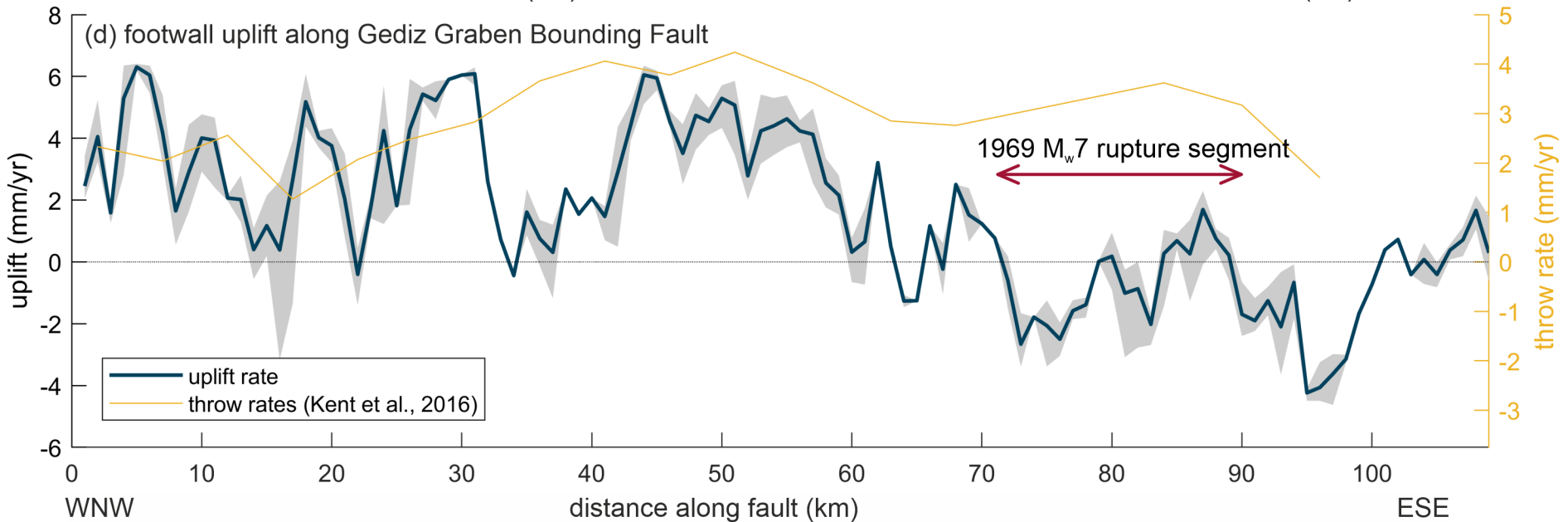
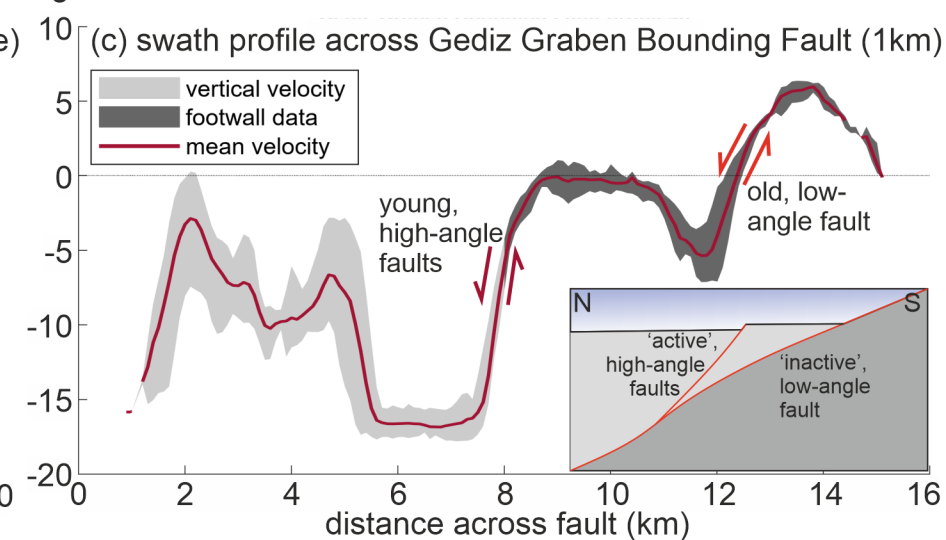
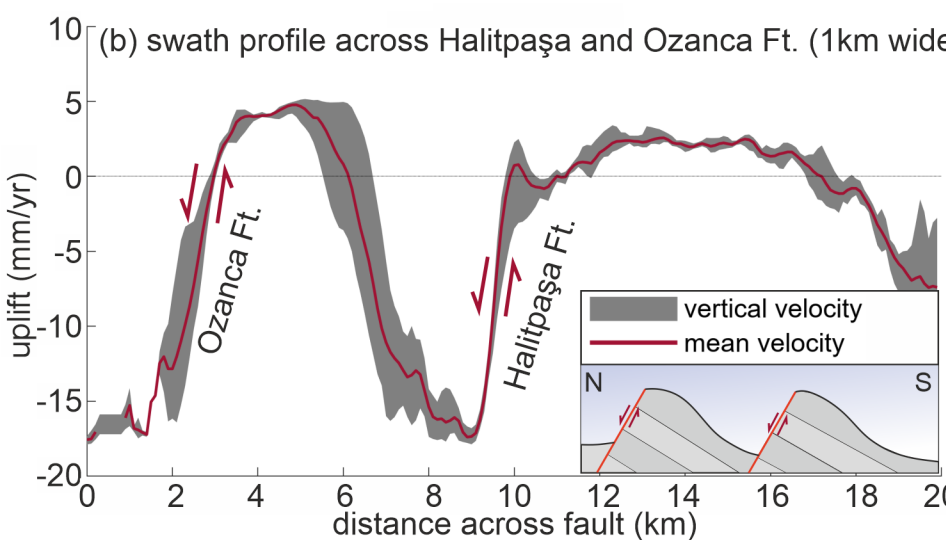
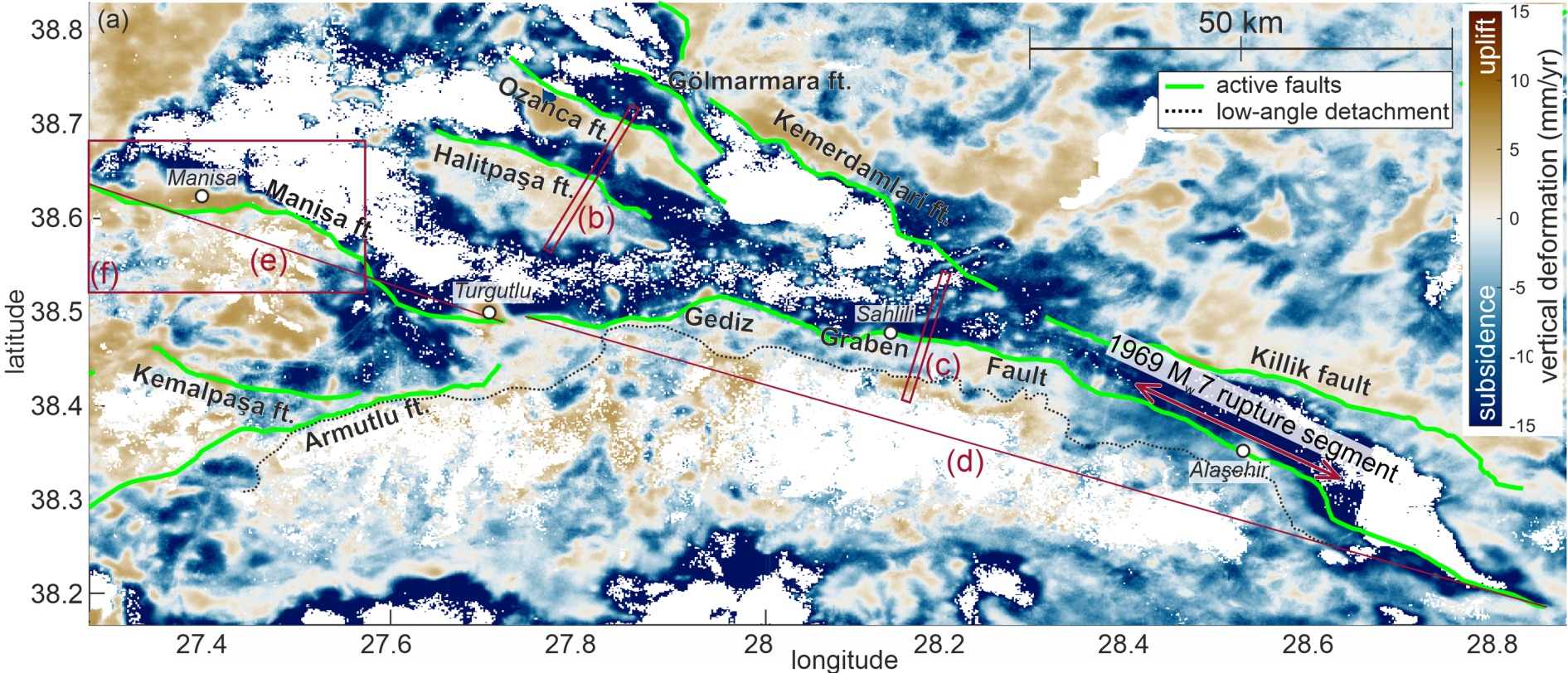


Figure 09.

